CHALMERS
UNIVERSITY OF TECHNOLOGY

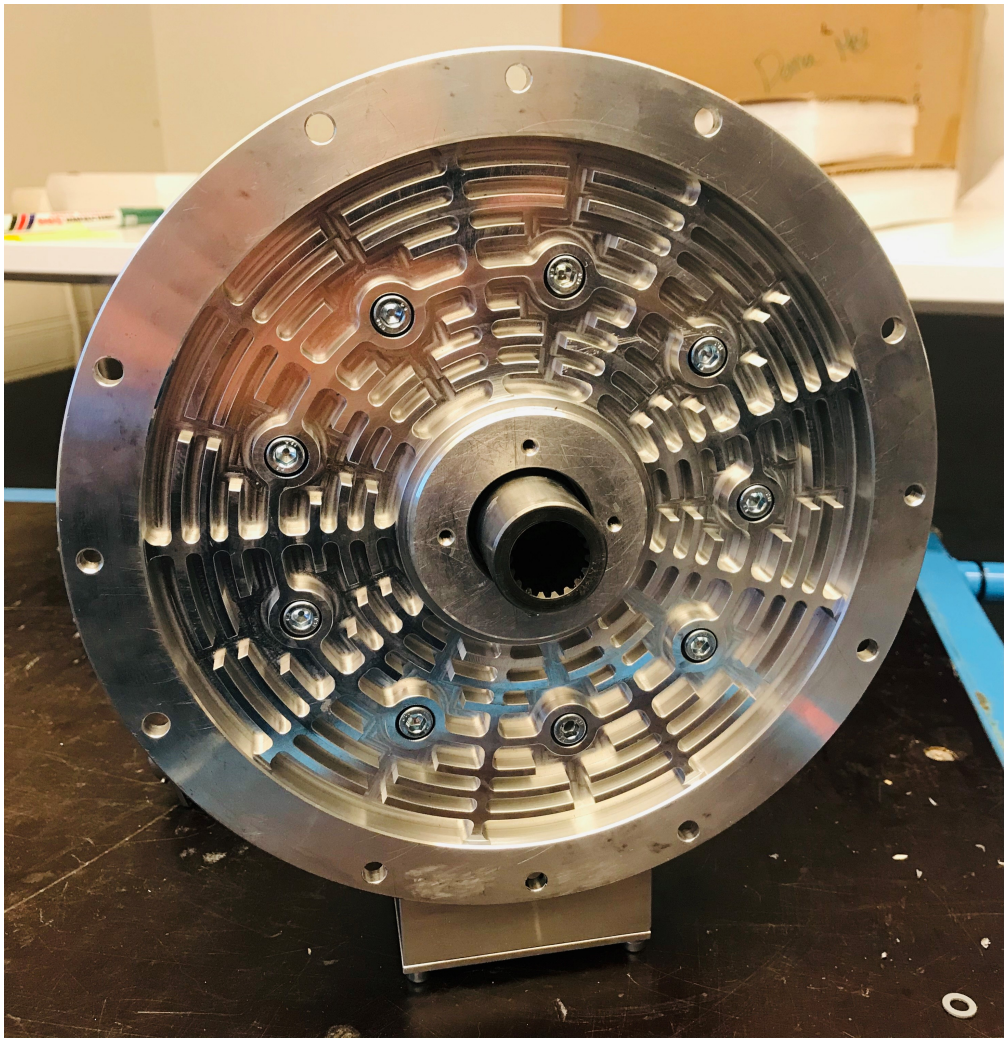

Modeling an Axial Flux Machine

Master of Science Thesis

DANA MEZHER

Department of Electrical Engineering
CHALMERS UNIVERSITY OF TECHNOLOGY
Gothenburg, Sweden 2022

Master's thesis 2020:2021

Modeling an Axial Flux Machine

DANA MEZHER

CHALMERS
UNIVERSITY OF TECHNOLOGY

Department of Electrical Engineering Chalmers University of Technology
Gothenburg, Sweden 2022

Modeling of an Axial Flux Machine
Dana Mezher

Supervisor: Sonja Lundmark, Department of Electrical Power Engineering
Examiner: Torbjörn Thiringer, Department of Electrical Power Engineering

Master's Thesis 2020:2021
Department of Electrical Engineering
Division of Electric Power Engineering
Chalmers University of Technology
SE-412 96 Gothenburg
Telephone +46 31 772 1000

Cover: Picture of the tested Axial Flux Machine.

Typeset in LaTeX
Printed by Chalmers Reproservice
Gothenburg, Sweden 2022

Modelling of an Axial Flux Machine
Validation of the simulated model versus the Axial Flux Machine lab testing results
Dana Mezher
Department of Electric Engineering
Chalmers University of Technology

Abstract

The development of electric motors has become one of the significant aspects of modern living. Many studies are performed continuously to find better solutions to improve the motor's shape, sizes, and power efficiency. This study contributes to the improvement of the Axial Flux Machines (AFM) that is used in many applications related to electric vehicles that require high efficiency and high-power density. The AFM model characteristics have many significant benefits compared to other types of electric vehicle machines, which is due to its electromagnetics, winding, and thermal features. Thus, the study of the performance of the AFM will add benefits to the future industry of electric vehicles.

A thorough analysis is conducted on two identical 4kW Axial Flux Permanent Magnet machines (AFPM), where one of the machines is dismantled to verify its geometry, and the other machine is used to perform experimental analysis. The obtained geometry is used to implement the AFPM machine using the Finite Element Method (FEM). Consequently, the experimental results are compared to the numerical results in order to verify the similarities of both models.

The AFM is tested for two main cases: open-circuit test and load test. The tests are performed for three selected speed references of 500rpm, 1000rpm, and 1500rpm. These cases are applied for the experimental and simulated tests to obtain the induced voltages and torques for further comparison.

The final results prove that both the experiment machine and the modelled machine are behaving similarly with a percentage error that is less than 15%. The difference in comparison is expected due to errors in determining the exact materials and measurements of the experiment machine.

Keywords: Axial Flux Machines, Permanent Magnet Machines, Simulation, Electric vehicles, Machine analysis.

Acknowledgements

The work of this thesis could not have been achieved without the help of the following individuals:

Torbjörn Thiringer (examiner, Chalmers University of Technology) – His consistent guidance and constant assessment during the whole project have deeply contributed to the completion of this thesis.

Sonja Lundmark (supervisor, Chalmers University of Technology) – Her assistance and intensive knowledge of modeling and designing techniques have highly supported my work.

Anders Hedebjörn (Volvo Car Group) – His invaluable guidance in installing and dismantling the motor has greatly helped the testing process.

Vineetha Puttarag (Chalmers University of Technology) – Her support with the simulation made the thesis easier and more exciting. I also appreciate her help in providing me with her measured stator resistance test outcomes.

Xiaoliang Huang and **Stefan Lundberg** (Chalmers University of Technology) – Their experience and contribution in lab testing and machine setup are much appreciated.

Junfei Tang (Chalmers University of Technology) – Finite element simulations could not have been facilitated without his modeling tutorials.

I am extremely grateful to my family and friends for their support throughout the thesis duration.

Dana Mezher, Gothenburg, December 2021

Contents

Abbreviations

AC	Alternating Current
AFM	Axial Flux Machine
AFPM	Axial Flux Permanent Magnet
AFPMSM	Axial Flux Permanent Magnet Synchronous Machine
Back-EMF	Back-Electromotive Force
BLDC	Brushless Direct Current Machines
DC	Direct Current
EV	Electric Vehicle
FEA	Finite Element Analysis
FEM	Finite Element Method
FFT	Fast Fourier Transform
FOC	Field-Oriented Control
FSCW	Fractional-Slot Concentrated Winding
FW	Flux Weakening
GCD	Greatest Common Divisor
ICE	Internal Combustion Engines
MMF	Magnetomotive Force
MTPA	Maximum Torque Per Ampere
PMSM	Permanent Magnet Synchronous Machines
RFM	Radial Flux Machine
RFPM	Radial Flux Permanent Magnet
RMS	Root Mean Square
YASA	Yokeless and Segmented Armature

Symbols

A	Area	m^2
A_m	The line current density	(A/m^2)
a_i	Factor between average and peak magnetic flux densities	
a_p	Number of parallel currents	
a_w	Number of parallel conductors	
B	Magnetic flux density	(T)
b_p	Pole width	(m)
D_i	Inner diameter	(m)
D_0	Outer diameter	(m)
d	Thickness	(m)
e	Back-Emf	(v)
f	Frequency	(Hz)
H_c	Magnetic coercivity	(A/m)
i	Current	(A)
I_a	Armature current	(A)
I_{ph}	Phase current	(A)
K	Fill factor	
k_{ex}	Excess loss coefficient	
k_{hys}	Hysteresis loss coefficient	
k_w	Winding factor	
L	Inductance	(H)
l	length	(m)
m_1	Number of phases	
m_a	Amplitude modulation ratio	
n	Harmonic number	
n_c	Number of coils per phase	
N	Number of turns in a coil	
N_{ph}	Number of conductors per phase	

Symbols

N_s	Number of stator segments	
P	Power	(W)
p	Number of pole pairs	
Q	Electrical loading	(A/m)
R	Resistance	(Ω)
R_i	Inner radius	(m)
R_0	Outer radius	(m)
$\Re$	Magnetic reluctance	(At/Wb)
r	Radius	(m)
S_i	Number of stator slot	
u	Voltage	(V)
z	Number of coils in a group	
w_{el}	Electrical angular frequency	(rad/s)
μ	Permeability	(H/m)
μ	Zero vacuum permeability	(H/m)
ψ_m	Magnetic flux linkage	(Wb)
ϕ	Displacement angle	(degrees)
θ_{mn}	Coil span angle	(degrees)
θ_{ps}	Phase-shift angle	(degrees)
ϕ_g	Air-gap flux density	(Wb)
ϕ_r	Magnetic flux density of rotor back	(Wb)
β_p	Pole-pitch angle	(degrees)
β_s	Slot-pitch angle	(degrees)
τ	Pole pitch	(m)
σ	Electric Conductivity of the conductors	(S/m)
η	Efficiency	(%)

1

Introduction

1.1 Problem background

Machines and apparatus that are running on electricity can play quite a vital role in our daily lives. Therefore, the need to conduct research to keep coming up with novel models that are better in shape, size, and efficiency is taking an upward trend. An axial flux machine is a type of geometry structure of an electric motor, where the magnets of this machine are placed between the stator and rotor in parallel with the rotation axis. The most common types of electric motor applications can be listed into two main classifications: axial flux motors and radial flux motors. In recent times, electrical machine studies have focused on axial flux machines, which can be significantly used in applications where high efficiency and high torque density are needed. Due to their high power density, axial flux motors are becoming more appealing regarding applications in electric vehicles. There are many benefits and downsides of using the axial flux machines (AFM) compared to the radial flux machines (RFM) when viewing their structure, electromagnetic, winding, and thermal features. Generally, AFM can be manufactured to be light in weight and short in axial length when compared to RFM, which is an advantage for electric vehicle applications [1]. However, several feasible solutions are conducted to improve both the AFM and RFM in terms of geometry and performance; thus, a general comparison may seem challenging to achieve [2].

By having two identical state-of-the-art 4kW AFM's, a thorough analysis is carried out in this thesis. One of the machines is dismantled to determine the machine's

geometry for further analysis. The other machine is used for conducting measurements that are compared to the results obtained from a model. Subsequently, the acquired geometry is used to implement the AFM using a Finite Element Method (FEM) software. The results taken from both lab measurements and modeling are then be compared.

1.2 Previous work

To the best of the author's knowledge, previous related work on dismantling, designing, and experimenting an axial flux machine is not found. Therefore, the following section includes previous work that is used to improve the understanding of the performance and analysis of the axial flux machines. The papers include information about; a comparison between the structure of the radial flux and axial flux machines with a recommendation of which of the machines is better used based on the demand, another comparison between the axial flux machine and the radial flux machine under low-speed performance, and a parametric study of the axial flux machine in regards to the length of the air gap, the thickness of the inner heat extraction fin, and the thickness of the permanent magnets.

Firstly, Cavingnino et al. [2] executed a comprehensive design evaluation amongst the Radial Flux Permanent Magnet (RFPM) machine and a Kaman machine, which is a type of an Axial Flux Permanent Magnet (AFPM) motor, with a direct drive application purpose. Both the RFPM and the Kaman had slotted stators and sinusoidal back-Electromotive Force (back-EMF). The basis of the comparison between the two machines comes from the following: identical volume, identical air-gap, identical heat loss with exchanged surfaces, yoke flux and teeth densities, and the identical valued speed of 1000 revolutions per minute (RPM). It is concluded that Cavingnino et al. [2] find that the AFPM topology is recommended when the pole pairs are sufficient, higher than 5 number of pole pairs. Additionally, the AFPM is recommended if the axial span is short in a way that the ratio between the axial span over the outer diameter is less than 0.3.

Furthermore, Parviainen et al. [3] executed a comparable assessment amongst a 55 kW radial and double-stator machines, a single-rotor machine, and an axial-flux machine with rated speeds of 150, 300, and 600 rounds per minute. A point worth mentioning about this comparison is the inclusion of mechanical constraints. The evaluation is done while taking into consideration the following aspects: cost, total volume, and efficiency. It is concluded that the radial flux machine is the most suitable due to the extended end windings of the axial flux topology. AFPM with single or double pole pairs recorded inefficient performance, additionally, it is determined that a wider variety of pole pairs can be used for radial flux machines. Nevertheless, machines that have more than eight pole pairs cost more in radial flux machines set-ups than in axial flux machines set-ups. Several pros and cons can be derived from the previously mentioned work, and, as a result, no general conclusion can be made.

Another paper [4] discusses the influence of geometrical parameters on the steady state average temperature of the stator core, the Axial Flux Permanent Magnet Synchronous Machine (AFPMSM), and the winding and the permanent magnets of the Yokeless and Segmented Armature (YASA). The geometrical parameters that were picked for the study include the air-gap length,and permanent magnet thickness. These selected parameters provide a better perspective on the efficiency and power density aspects. Additionally, this study is beneficial for analysing the connection between the values of geometrical parameters, while keeping in mind detailed performance criteria. The criteria includes maintaining a required minimum efficiency, assigning limits on maximum temperature for some parts to extend their lifetime duration, and determining the speed range of the parts to maintain the proper temperatures and keep them below the critical values. These considerations are crucial for synchronous machines since the speed rate affects heat transfer and losses convection coefficients. Another important point is the direct effect of the air-gap on the overall machine losses and its convection coefficient that results in varying machine's temperatures. Furthermore, the effect of temperature is taken into consideration while keeping the speed variation in mind, which influences the

machine's losses and convection coefficients. Consequently, all the tested parameters are performed using the YASA AFPMSM in comparison with a commercially driven induction machine [4].

Finally, It is found that the air-gap length variations and speed affect the sensitivity of the core temperature and the winding, more than the PM temperature.

1.3 Purpose

The target of this thesis is to compare the real measured readings with the ones generated by the implemented axial flux machine by using a FEM software.

1.4 Scope

This thesis will include laboratory testing of an axial flux machine followed by verifying results using a FEM software. The modelling tools will depend on the geometry obtained from dismantling the machine along with the supporting analytical analysis. The analytical study will be performed to provide a better understanding of the equations used during the modelling process and results. Based on the applied geometry parameters, the results will be verified accordingly.

Due to time constraints, there will be no analytical and modeling comparison between the radial flux machine and the axial flux machine. Also, the modeling results are not expected to match precisely the compared measured analysis due to the uncertainty in determining the exact parameters and material constants of the machine.

2

Axial flux permanent magnet synchronous machines

2.1 Fundamentals of permanent magnet machines

The theory of torque production and the expected waveform of permanent magnet machines are briefly introduced in this section. Torque calculations can be determined using two approaches; using electromagnetic force and using the multiplication product of magnetic and electric loading.

2.1.1 Torque production in axial flux machines

The first part of this section covers the torque production using electromagnetic force. Unlike cylindrical machines with constant radius, the electromagnetic torque for AFM is produced over a field of radii. The pole width $b_p(r)$ and pitch $\tau(r)$ of the AFM are functions of the radius, r, as shown in [5]

$$b_p(r) = a_i \tau(r) = a_i \frac{\pi r}{p} \tag{2.1}$$

$$\tau(r) = \frac{2\pi r}{2p} = \frac{\pi r}{p} \tag{2.2}$$

where p is the number of pole pairs, and a_i is the pole angle in radians, which gives the ratio between the magnetic flux densities in the air gap; average B_{avg} and the peak value B_{mg}, as shown in

$$a_i = \frac{B_{avg}}{B_{mg}} \tag{2.3}$$

Additionally, the peak line current density A_m as a function of the radius can be given as follows

$$A_m(r) = \frac{m_1\sqrt{2}N_1I_a}{p\tau(r)} = \frac{m_1\sqrt{2}N_1I_a}{\pi r} \tag{2.4}$$

where m_1 is the number of phases, N_1 is the number of turns in series per phase, and I_a is the armature current in Root Mean Square (RMS). Using Ampere's equation, the tangential force can be calculated as

$$dF_x = I_a(dr \times B_g) = A(r)(dS \times B_g) \tag{2.5}$$

From (2.5), $I_a dr = A(r)dS$ where dr and dS are the radius element and the surface element, respectively. B_g is the perpendicular vector component to the disc surface of the magnetic flux density, which does not depend on the radius for disc type of AFPM machines. From (2.3) and using $dS = 2\pi r dr$, the electromagnetic torque from (2.5) becomes [5]

$$dT_d = rdF_x = r[k_{w1}A(r)B_{avg}dS] = 2\pi a_i k_{w1}A(r)B_{mg}r^2dr \tag{2.6}$$

For distributed stator windings, the line current density $A(r)$ is the electric loading per unit stator active surface. While for internal toroidal or coreless stators, $A(r)$ is the electric loading for the entire stator. k_{w1} is the winding factor. From (2.4) and (2.6), AFPM motor produces an average electromagnetic torque calculated as

$$dT_d = 2a_i m_1 I_a N_1 k_{w1} B_{mg} r dr \tag{2.7}$$

When (2.7) is integrated with respect to the radius, the average electromagnetic torque can be calculated as

$$\begin{aligned} T_d &= \frac{1}{4} a_i m_1 I_a N_1 k_{w1} B_{mg} (D_o^2 - D_i^2) \\ &= \frac{1}{4} a_i m_1 I_a N_1 k_{w1} B_{mg} D_o^2 (1 - k_d^2) I_a \end{aligned} \tag{2.8}$$

where $k_d = \frac{D_i}{D_o}$. Moving to the second approach, the torque is calculated using the multiple between magnetic and electric loading. According to publications from [6] and [7], the electromagnetic force on the rotor is calculated as

$$F_x = \pi B_{avg} A (R_o^2 - R_i^2) \tag{2.9}$$

where the average magnetic flux B_{avg} represents the magnetic loading and the rms line current density A represents the electric loading at the inner radius. The product $B_{avg}A$ is then multiplied by the active surface of the permanent magnet $S = \pi(R_o^2 - R_i^2)$ and thus the electromagnetic torque is calculated as [5]

$$T_d = F_x R_i = 2\pi B_{avg} A (R_o^2 - R_i^2) R_i = 2\pi B_{avg} A R_o^3 (k_d - k_d^3) \tag{2.10}$$

2.1.2 Waveform characteristics

Permanent magnet machines are categorized into two types of machines based on their waveform characteristics. The first is the Brushless Direct Current Machines (BLDC) and Permanent Magnet Synchronous Machines (PMSM). For the PMSM, the waveform of the current and back-EMF are sinusoidal, while it is trapezoidal or square for the BLDC machines in terms of the back-EMF, and square in terms of currents. Figure 2.1 shows the waveforms of BLDC where it can be seen that the shape of the air-gap magnetic flux density B_m is quasi-sqare [8]. The PM flux linkage ψ_m for a winding that covers 60^o is calculated from

$$\psi_m(\theta) = \int_{\theta_m - 30}^{\theta_m + 30} B_m(\theta_m) d\theta_m \tag{2.11}$$

Additionally, the back-emf in Figure 2.1 with a square shape, is calculated from the time derivative of the flux linkage based on Faraday's Law, as in

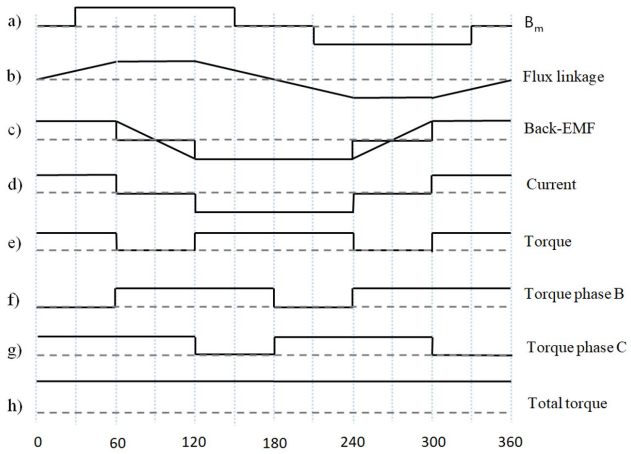

Figure 2.1: Ideal waveforms of a BLDC machine.

$$e = \frac{d\psi_m}{dt} \tag{2.12}$$

The current is related to the torque; hence, if the current follows the transition of the back-emf polarities, the result is a positive product, which is related to the power and torque by one phase, as presented in Figure 2.1. Consequently, for the other two phases in a three-phase machine, the produced torque is shifted by 120^o and 240^o [8]. The total torque of the machine is equal to the torque produced by all of the three phases, presented as a constant value in Figure 2.1.

Even though the air-gap flux density and the winding distribution are not sinusoidal in reality, their combination results in a lower harmonic content for the PMSM. This means that if the air-gap flux density is of a square shape, the windings arrangement is changed to sinusoidal distribution in order to achieve a sinusoidal flux linkage. Additionally, changing the discretized geometry of the BLDC, to form a sinusoidal air-gap flux density, results in a sinusoidal flux linkage for PMSM. Hence, the same winding configuration for the BLDC can be used without any changes [8].

2.2 Theoretical background of axial flux permanent magnet machines

The geometry of the permanent magnet axial flux machine is explained in the following cylindrical coordinate system, shown in Figure 2.2. The machine is located around the z-axis, hence the axial length is described in the z-axis direction. Additionally, the rotating parts of the machine rotate around the z-axis in a $\pm\theta$ direction, therefore, the quantities of the machine are described in the radial direction which is parallel to the xy-plane, shown as r in Figure 2.2 [8].

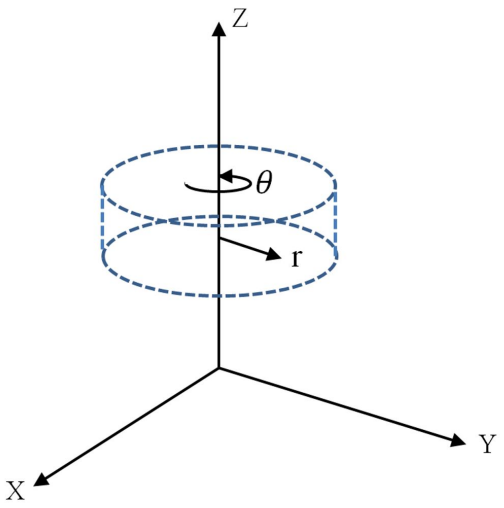

Figure 2.2: Axial flux machine in a cylindrical coordinate system.

2.2.1 Different Topologies of axial flux machines

Different configurations can be applied in axial flux machines. All configurations share the fact that the magnetic flux flows in an axial direction through the air-gap. However, there are variations that correspond to the mechanical and electromagnetic designs such as; permanent magnets, induction, interior permanent magnets, brushed DC, and switched reluctance machines. In this thesis, the main consideration is permanent magnet machines, which has comparable similarities to the other electromagnetic machines when compared to radial designs [9]. Figure 2.3 shows

the 4 main different topologies of axial flux machines.

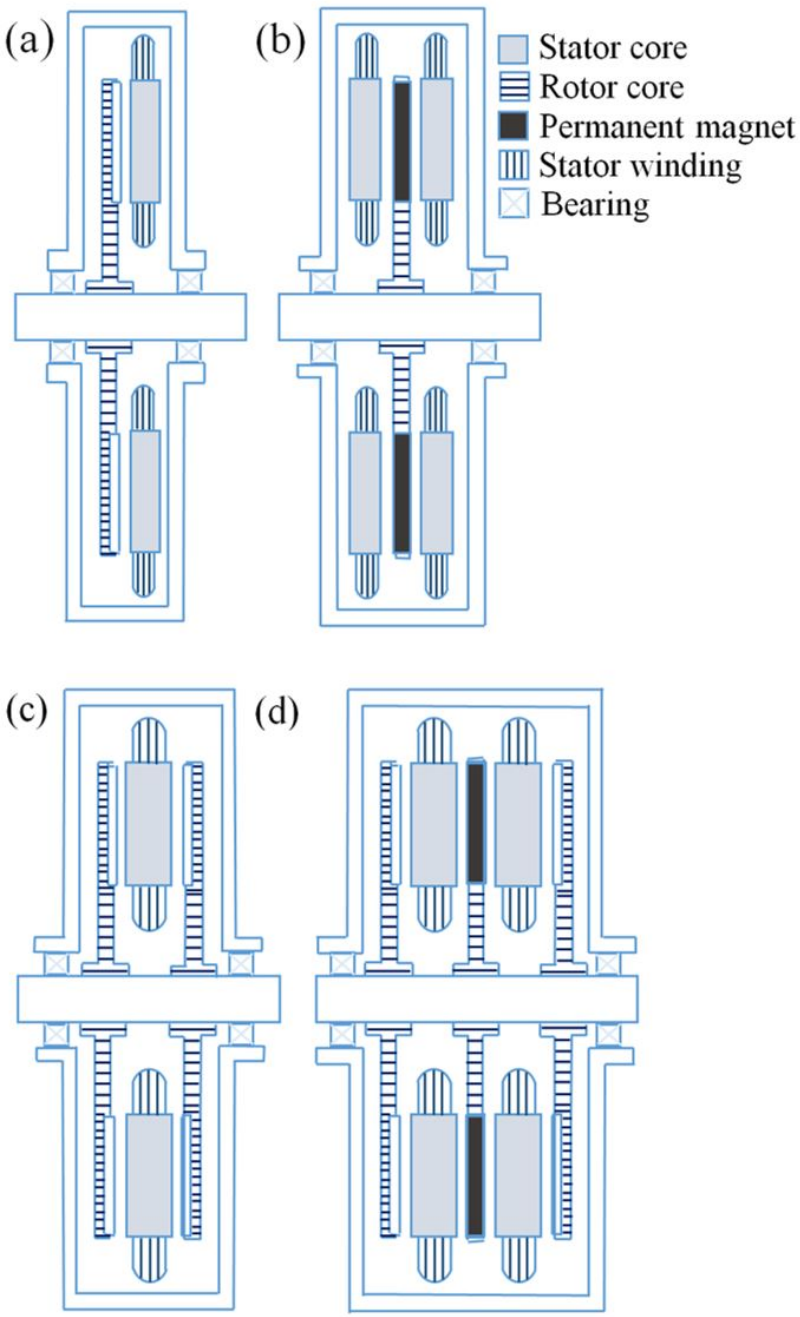

Figure 2.3: Four basic AFM topologies: a) Single-sided b) Inner rotor dual sided stator c) Inner stator dual sided rotor d) Multi-disc

2.2.1.1 Single sided AFM

Figure 2.3-a shows a single sided machine that is composed of one stator and one rotor that are facing each other. Such machines have the lowest part count, and as

a result, have the lowest power due to having only a single active air gap. If the machine has no air gap and instead has a higher copper content in the winding; the changes will still be minor due to the fact that only one side of the stator is accessible for cooling. Additionally, another drawback is the attraction force between the stator and rotor, which can be a few kN in magnitude [5]. When it comes to cooling; these machines are either air cooled or heat drained from the stator by using indirect cooling at the back of the stator. These mentioned ways of cooling allow conventional methods, such as using water and glycol, in addition to allowing the machine to integrate into a cooling circuit that is shared with powertrain components [9].

2.2.1.2 Inner rotor dual sided stator AFM

This type of machines, which is also known as central rotor machines, are composed of two stators that are separated by a single PM disc rotor in their center, as presented in figure 2.3-b. Central rotor machines are also considered two single sided machines that are merged together with a yokeless rotor. Such rotors could be created using magnetic and non-magnetic substances. The PM could be surface mounted or interior mounted into the rotor skeleton [10]. An interaction takes place over the two air gaps with the two stators when the flux passes through the rotor. Due to the cooling accessibility to the two stator faces, this configuration doubles the cooling area, which results in an increase of power output. Moreover, conventional coolant can be used to provide indirect cooling to the stators. Additionally for this configuration, the non-rotating components are placed on the outer part of the machine, which allows simpler integration into vehicle chassis [9]. The stators are still functional in parallel-connected stators, even in the case that one of the stator windings might be damaged. Series-connected stators provide equal and opposite axial attractive forces, which is favored [10].

2.2.1.3 Inner stator dual sided rotor and Multi disc AFM

Multi disc AFM or central machines are composed of one stator that is placed between two rotors. The difference from the machines in section 2.2.1.2 is that

these machines require rotors with keeper disks, known as yokes, which acts as return routes for the magnetic flux, as presented in Figure 2.3-d. Nevertheless, there are two main disadvantages of these machines. The first being its difficulty to integrate in a vehicle chassis due to the presence of two rotating disks with a static stator between them. The second is the difficulty of providing indirect cooling to the stator. In this case, direct liquid cooling provides optimum performance [10]. Otherwise, another method is to circulate air through the machine, but this has a reduced power output [9].

2.3 Analytic methods

When designing an axial flux machine, analytical and numerical methods are followed. The theory behind the analytical methods is explained in this section. For more accurate results, finite element analysis (FEA) numerical methods can be applied. ANSYS Maxwell FEA software is used. This section includes the main elements when designing the axial flux machine.

2.3.1 Machine features in the dq-coordinate system

The PMSM stator has three armature windings, where the rotor is equipped with permanent magnets and the windings are star-connected. Three-phase symmetrical sinusoidal wave currents flow into the stator. This creates a rotating magnetic field, which causes the rotor to rotate as a result of the interaction with the rotor magnetic field [11]. Figure 2.4 [12] shows the d-q model of transformation for the PMSM.

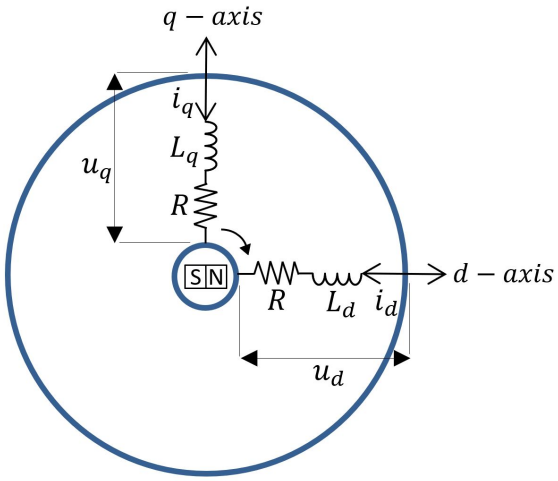

Figure 2.4: PMSM d-q model of transformation

The equivalent resistance R is considered for a single winding. The equivalent voltages u_d and u_q, the equivalent currents i_d and i_q and the equivalent inductances L_d and L_q are in d-axis and q-axis, respectively. The voltages satisfy the voltage equation in the d-q system as [12]

$$u_d = Ri_d + L_d\frac{di_d}{dt} - \omega_{el}L_q i_q \tag{2.13}$$

$$u_q = Ri_q + L_q\frac{di_q}{dt} + \omega_{el}L_d i_d + \omega_{el}\psi_m \tag{2.14}$$

where ψ_m is the magnetic flux of the stator and ω_{el} is the electrical angular frequency of the rotor. The inductances can be expressed as [12]

$$\begin{aligned} L_d &= \frac{3}{2}(L_{a0} - L_{a2}) \\ L_q &= \frac{3}{2}(L_{a0} + L_{a2}) \end{aligned} \tag{2.15}$$

L_{a0} is the inductance mean of the stator and L_{a2} is the second harmonic amplitude of the stator inductance. The following is used to calculate the phase voltage, as

$$u = \sqrt{u_d^2 + u_q^2} \tag{2.16}$$

If the inductances in the d-axis and q-axis are assumed to be equal, $L_d = L_q = L$, the resistance is ignored, and by combining (2.13), (2.14) and (2.16)

$$(\frac{u}{\omega_{el}L})^2 = i_q^2 + (\frac{\psi_m}{L} + i_d)^2 \tag{2.17}$$

Figure 2.5 shows the voltage limit circles in the $i_d i_q$- plane (dashed circles), assuming that the voltage u from (2.17), is the maximal available voltage [13]. The center of the circles is point $-\psi_m/L$ on d-axis, and the circles' radii are equal to $u/\omega_{el}L$, which means they are inversely proportional to the electrical angular frequency.

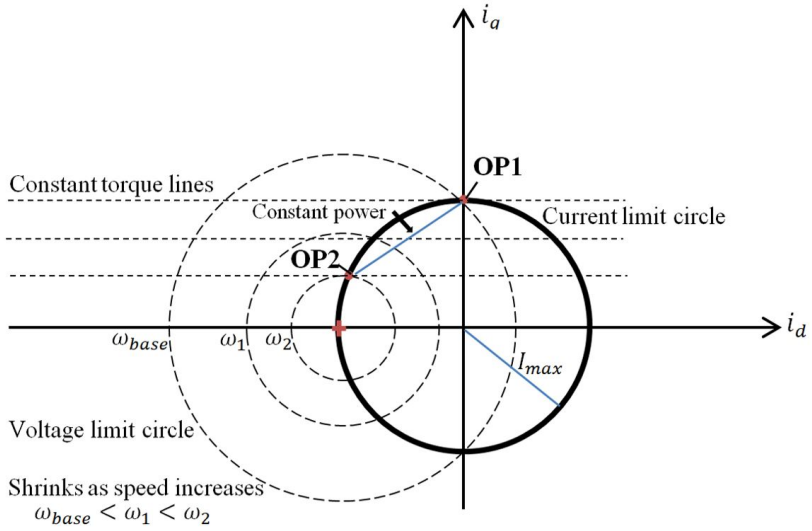

Figure 2.5: Current and voltage limit circles in dq-plane.

The phase current can be computed as follows

$$i = \sqrt{i_d^2 + i_q^2} \tag{2.18}$$

which is visualized as the current limit circle in Figure 2.5 if i is considered as the maximal current. The center of the current limit circle lies on the origin of the dq-plane. The general equation of electromagnetic torque produced from a PMSM is a multiplication of the permanent magnet flux and its current [12], as in

$$T = \psi_m i_q + (L_d - L_q) i_d i_q \tag{2.19}$$

However, if it can be assumed that the inductances, L_d and L_q are equal due to a non-salient machine, the second term of the equation is zero. Therefore, the torque equation only contains the first term, and is proportional to the i_q component as

shown in

$$T = \psi_m i_q \tag{2.20}$$

The electromagnetic torque can be modified by changing the current in q-axis, since the amplitude of the permanent magnet flux is a specific parameter of the motor and cannot be modified. The horizontal dashed lines, in Figure 2.5 are the constant torque lines in the dq- plane [12], [8].

2.3.2 Flux weakening control

For automotive PMSM-drive systems, a field weakening control is used to provide a wide constant power-speed range. The way the field weakening control operates is when the back-EMF exceeds the maximum output voltage of the drive, the PMSM will not allow current to be controlled in, and as a result, the torque will not be controlled. Therefore, the air-gap flux can be weakened in order to achieve an extended speed of the rotor after the back-EMF reaches the maximum voltage [14]. At a certain speed, a permissible operating point (OP) must be within both the current and the corresponding voltage limit circles. Theoretically, the machine can operate at infinite speeds if $-\psi_m/L$, which is the center of the voltage limit circle, lies inside or on the boundary of the current limit circle. In Figure 2.5, OP1 corresponds to the rated torque and the rated speed operating point, as the torque is constant when the speed starts from zero up to a rated speed. From (2.20), it can be seen that only the current in q-axis needs to be fed into the machine, resulting in the desired torque. This is explained in Figure 2.6, which shows the general torque-speed relationship of the machine. Up to the rated speed, the first region is referred to as the constant torque region. Above the rated speed, the second region shows the flux-weakening region. As the speed increases beyond the rated speed, a negative current in the d-axis is applied to move the operating point into the voltage limit circle. Due to this, the current in the q-axis is reduced in order to remain within the current limit circle. This is indicated as OP2, which is an example of a field weakening point reaching maximum torque, as shown in Figure 2.5.

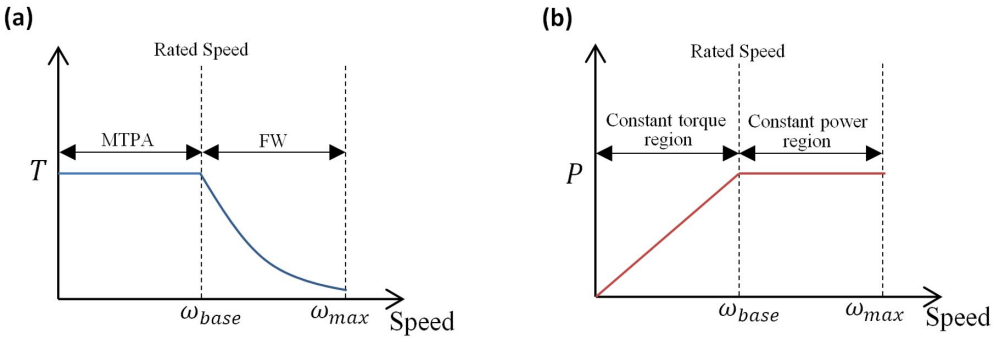

Figure 2.6: Torque and power characteristics of PMSM: a) torque vs speed, b) power vs speed.

The second region is also referred to as the constant power region, from Figure 2.6-b. However the power is not constant, since it is the product of the increasing speed (ω) and the decreasing torque (T), as

$$P = T\omega \tag{2.21}$$

Figure 2.7 shows the phasor diagrams of the voltage for three operating points, where φ is the displacement power factor between the voltage and the currents. The maximum displacement power factor $|\cos(\varphi)|$, below rated speed in Figure 2.7 -a is $\frac{1}{\sqrt{2}} = 0.71$. When the speed increases beyond rated speed, the phase displacement between the current and voltage decreases. Thus, the power factor increases in the field weakening region, as seen in Figure 2.7-c [8]. Additionally, the blue lines showed in Figure 2.7-c, presents the voltage when including a resistive component.

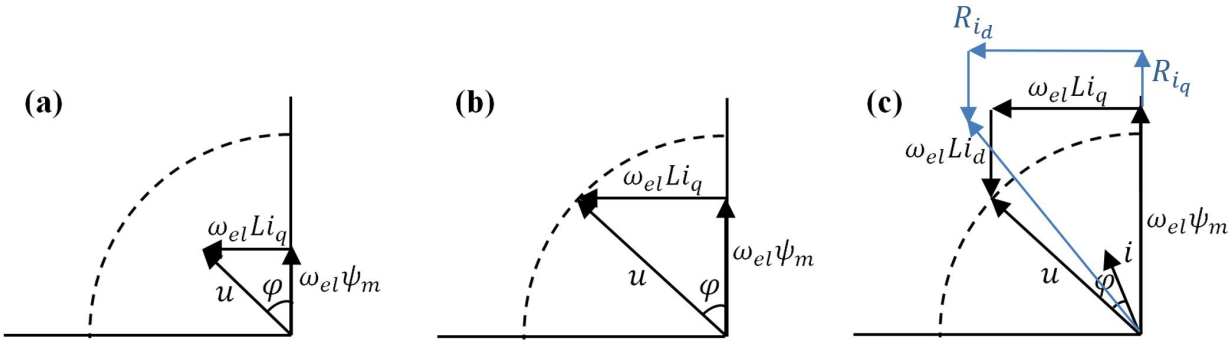

Figure 2.7: Voltage phasor diagrams: a) below rated speed, b) at rated speed, c) field weakening

2.3.3 Voltage limit

The maximum value of the fundamental frequency voltage component, corresponding to the neutral of the 3-phase inverter leg, is equal to $U_d/2$, thus, the maximum RMS value of the fundamental line-to-line voltage is expressed as [5]

$$U_{LL-1-rms} = \frac{\sqrt{3}}{2\sqrt{2}} m_a U_d = 0.612 m_a U_d \tag{2.22}$$

where U_d is the constant input voltage. The amplitude modulation ratio is denoted as m_a and computed as:

$$m_a = \frac{\hat{U}_{control}}{\hat{U}_{tri}} \tag{2.23}$$

where $\hat{U}_{control}$ is maximum amplitude of the control signal and $\hat{U}_{tri}$ is the constant triangular signal, as explained by [15]. The relationship between this modulation ratio and the fundamental-frequency component in the output voltage is linear when

$$m_a \leq 1 \tag{2.24}$$

This is referred to as the linear region. This region is increased by 15% when the third harmonic is added to the phase voltage. Therefore, the maximum phase voltage is rewritten as:

$$\hat{U}_{ph-1} = 1.15 \frac{U_d}{2} m_a \tag{2.25}$$

2.3.4 Winding elements and winding factors

Windings types include overlap and non-overlap windings. The latter type indicates that each coil is wound around a tooth so that the end windings do not overlap, which is also called concentrated windings. Furthermore, they can be either [5]:

- Single or double layered
- Concentrated or distributed
- Integral or fractional

- Air-cored or iron-cored

The focus type of windings in this thesis is non-overlap Fractional-Slot Concentrated Windings (FSCW) that is double-layered and iron-cored, meaning a slot is shared by two non-overlapping stator coils. The number of slots per pole per phase in FSCW varies between different poles, which may lead to the production of high-speed subharmonics rotation of the rotor in the airgap. The average number of slots per pole per phase is treated as a function. The FSCW type is commonly used in bigger sized PMSM machines with a higher number of poles [16]. For double layered iron-cored windings there are two coils per slot. These windings are also known as tooth windings since the teeth are wound. Additionally, the number of stator coils is equal to the number of stator slots $N_s = n_c m_1 = s_1$, where N_s is the number of stator segments, n_c is the number of coils per phase, m_1 is the number of phases and s_1 is the number of stator slots. While in the single-layered windings, the number of coils is half the number of stator slots. As for the concentrated windings, each coil group represents a phase, thus it includes only one coil $z = 1$, where z is the number of coils in a group. Whereas, for the distributed windings, there are two or more coils in a coil group. For fractional windings the coils in a coil group are not evenly distributed, unlike in integral windings [5]. Non-overlap windings can be divided into a number of sections F that is repeated in every pole section and it is computed from the greatest common divisor (GCD) from the number of poles p and number of stator segments N_s [5] as in

$$F = GCD(2p, N_s) \tag{2.26}$$

where $2p/F$ is referred to as the number of poles per pole section. This indicates whether negative (uneven $2p/F$) or positive (even $2p/F$) periodic boundary conditions are used in FEA.

2.3.5 Torque computations

Torque computations differ slightly between slotted and non-slotted stators. This is due to the non-uniform reluctance of the air-gap. The causes of the non-uniformity

are related to the structure of stator slots, the space in the middle between PM poles and rotor, magnets' parallel magnetization and the stator's lamination material saturation. In addition, non-uniform reluctance can cause cogging torque due to the air-gap flux density variation in relation to the rotor placement [17]. The torque is computed using the magnetic and electrical loading multiplication, with consideration of the air-gap spaces as in

$$T = \pi B_{avg} A \frac{D_o + D_i}{2} D_i \frac{D_o - D_i}{2} \tag{2.27}$$

where A is the electrical loading calculated as

$$A = k_{w1} \frac{2 N_{ph} I_{ph}}{\pi D_i} \tag{2.28}$$

where I_{ph} is the phase current and N_{ph} is the number of conductors per phase. The magnetic loading B_{avg} is the average flux density over the rotor surface.

2.3.6 Rotor core length

When the external magnetic reluctance $\mathfrak{R}$ is greater than zero, energy forms in the external space with the rotor back of the permanent magnet. However, magnetic characteristics do not appear in the external space if the permanent magnet is magnetized beforehand and positioned inside a closed ideal ferromagnetic circuit. Even though the magnetic characteristics are not shown in rotor back external space, the magnetic flux exists [5], and the magnetic flux density in positive θ-direction is calculated from [5]

$$\phi_\theta = A_r B_\theta = l_\theta (R_o - R_i) B_\theta \tag{2.29}$$

where A_θ and B_θ are the cross-sectional area and the magnetic flux density in the rotor back, respectively. Figure 2.8 shows the cross-sectional area of the rotor with respect to the magnet, where l_θ is the length of the rotor. The total air-gap flux per pole, where the pole area is assumed to cover 2/3 of the magnet, is calculated from [5] and [8]

$$\phi_g = B_{pm} A_{pm} = \frac{2}{3} B_m \pi \frac{R_o^2 - R_i^2}{2p} \tag{2.30}$$

where $2p$ is the number of poles, and B_{pm} as well as A_{pm} are the flux density and area of the permanent magnet, respectively.

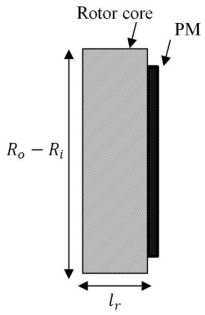

Figure 2.8: Cross-sectional area of the rotor back

Figure 2.9 shows the distribution of the air-gap flux density simplified into square shapes B_m if 2/3 of the pole pitch is covered by the permanent magnet [8].

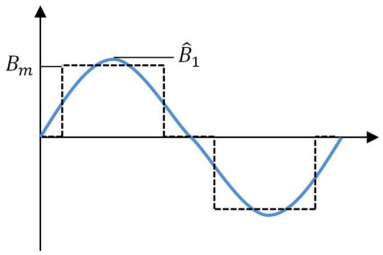

Figure 2.9: Air gap flux density distribution

The air-gap flux density ϕ_g is two times the magnetic flux of the rotor back ϕ_r as half of the flux per pole travels through the rotor back in positive θ-direction and the other half through the negative θ-direction. Using this relationship, combining (2.29) and (2.30), the length of the rotor core is calculated as

$$l_r = \frac{B_m}{B_\theta} \frac{\pi}{6p} (R_i + R_o) \tag{2.31}$$

2.3.7 Pole pairs and stator segments

Combinations relating to the numbers of feasible slots and poles are used for three-phase PMSM in order to obtain the required flux linkage. If the stator slot segment is not close to the number of poles, the magnetic flux of the motor will not be maximised as required. In addition, the number of slots N_s cannot be exactly equal to the number of poles $2p$ [18] and [15]. Thus, the relationship is expressed as follows

$$N_s = 2p \pm 1, 2p \pm 2 \tag{2.32}$$

The phase-belt angle, in relation to the number of poles and slots, is calculated in

$$\theta_{ps} = \beta_s \frac{N_s}{3} \frac{180}{\beta_p} = \frac{2p\beta_p}{N_s} (\frac{Ns}{3} \frac{180}{\beta_p}) = \frac{360p}{3} \tag{2.33}$$

The angle is equal to $\pm 360k + 120$ in electrical degrees and N_s is divided by 3 for a three-phase machine. β_p is the pole-pitch angle and the slot-pitch angle β_s is calculated in

$$\beta_s = \frac{2p\beta_p}{N_s} \tag{2.34}$$

The combinations can be found in Table 2.1 [8], noting that the number of slots per phase is odd for $N_s = 2p \pm 1$, while it is even for $N_s = 2p \pm 2$. When it is an odd number, the coils in one phase must be in series connection, and this is due to the EMF not being in phase. The number of coils increase in the series with the increase of p, which leads to a decrease in the winding factor. When the slots per phase is an even number, the coils may be in series connection or in groups of series/parallel (p is odd) or series/anti-parallel (p is even). Therefore, $N_s = 2p \pm 2$ combinations result in parallel paths that are greater than 1. New combinations can be obtained by multiplying N_s/p by a positive integer [18].

Table 2.1: Feasible pole and slot number combinations for a 3-phase machine [8]

Number of pole pairs p	$N_s = 2p \pm 1$	$N_s = 2p \pm 2$
1	3	-
2	3	6
4	9	6
5	9	12
7	15	12
8	15	18
10	21	18
11	21	24
13	27	24
14	27	30
16	33	30
⋮	⋮	⋮

The inverse of the smallest common multiple between p and N_s is related to the cogging torque. Moreover, different winding factors are a result of various slot combinations for a given pole-pairs number for harmonics (fundamental and high-order EMF) and armature reaction MMF distribution. Based on the mentioned above, the choice of a combination has an effect on the performance, demagnetization capability and the properties of noise/vibrations of the machine [18].

2.3.8 Inductances

In order to calculate the inductance of the coil, the magnetic circuit shown in Figure 2.10 is considered. The core is assumed to have a permeability μ that is larger than the vacuum permeability μ_0. In addition, the leakage flux is neglected, thus there is no fringing flux at the gap, and the flux passing through the core passes through the gap, as in

$$\phi_g = \phi_c \tag{2.35}$$

By first determining the field in the gap, the inductance is given as

$$L = \frac{\mu_o N^2 A_g}{l_g} \tag{2.36}$$

where N is the number of turns around the stator segment. The area A_g and the

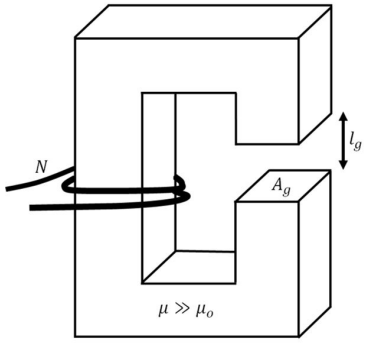

Figure 2.10: Magnetic circuit with current source.

length l_g of the air-gap are shown in Figure 2.10 [19]. If $N_s = 2p \pm 2$ is chosen for the stator segments number, the segments per phase are divided into pairs. To balance the attracting forces between the rotors and stator, the coils are series-connected around the pairs. The corresponding air-gap length l_g is calculated as [8]

$$l_g = 4(l_{pm} + l_{gs}) \tag{2.37}$$

where l_{pm} is the permanent magnet length and l_{gs} is the length of the air-gap between the stator segment and the permanent magnet for an inner stator-dual rotor AFM example. The approximate corresponding air-gap area A_g is calculated as the area of the stator segment shoe, which opposes the airgap [8] as in

$$A_g = \frac{\pi R_o^2}{N_s} - R_i^2 \tan\left(\frac{\pi}{N_s}\right) \tag{2.38}$$

After combining (2.36) with (2.37) and (2.38), the phase inductance for a three-phase machine, for the example of the inner stator and double rotor AFM, is calculated as

$$L_s = \frac{\mu_0(\pi R_0^2 - N_s R_i^2 tan(\frac{\pi}{N_s}))N^2}{6(l_{pm} + l_{gs})} \tag{2.39}$$

2.3.9 Power losses and efficiency

Copper and iron electromagnetic losses are calculated differently. The copper losses P_{cu} are calculated from [3]

$$P_{cu} = m_1 i_s^2 R_{DC} \tag{2.40}$$

where i_s is the phase current and R_{DC} is the resistance for winding per phase for the DC current is calculated as

$$R_{DC} = \frac{N_1 l_{1av}}{a_p a_w \sigma A} \tag{2.41}$$

where a_p is the number of current paths, a_w is the number of parallel conductors and σ is the electric conductivity of the conductor, which is approximately equal to $57 \times 10^6 S/m$ at $20^o C$ temperature and $47 \times 10^6 S/m$ at $75^o C$ temperature. A is the cross-section area of the conductor and N_1 is the number of turns per phase. The average length of turn l_{1av} is calculated as

$$l_{1av} = 2L_i + l_{1in} + l_{1out} \tag{2.42}$$

where l_{1in} and l_{1out} are the lengths of inner end connection and outer end connection, respectively, while L_i is the effective length of the stack. The equation for iron losses P_{Fe} per unit volume includes hysteresis, eddy current and excess losses sections [3] which are calculated from the Steinmetz equation as

$$P_{fe} = k_{hys} \hat{B}^2 f + \pi^2 \frac{\sigma_{fe} d^2}{6} \hat{B}^2 f^2 + 8.67 k_{ex} \hat{B}^{1.5} f^{1.5} \tag{2.43}$$

where k_{hys} is the hysteresis loss coefficient and k_{ex} is the excess loss coefficient, which are determined from curves as a function of frequency f. Moreover, σ_{Fe} is the electric conductivity of the lamination material and d is the thickness of the steel sheet. The efficiency equation is calculated as

$$\eta = \frac{P_{out}}{P_{in}} = \frac{P_{out}}{P_{out} + \Delta P} \tag{2.44}$$

where P_{out} and P_{in} are the mechanical output power and electrical input power and ΔP is the total power losses of an AFPM machine.

2.4 Sustainability aspect

Axial flux machines, which are powered by electrical batteries, reduce the emission of carbon dioxide compared to the Internal Combustion Engines (ICE) which run on fossil, such as; diesel/petrol that transfer chemical energy to mechanical energy causing high levels of carbon dioxide emission. Such atmospheric discharges have a critical impact on the surrounding environment. A research that was conducted by Emission Database for Global Atmospheric Research [20] estimated that about 14% of man-made carbon dioxide emissions are caused by vehicles and transportation related aspects. Various solutions are recommended to reduce the impact which include minimizing and even eliminating, if possible, the usage of fossil fuels as a source of energy, while a second solution is equipping vehicles with electric batteries to reduce carbon dioxide discharges. However, the first solution is rather costly, while the second is not fully applicable yet [21].

2.4.1 Ecological aspects

When it comes to ecological aspects; the commercialization of lithium-ion batteries expanded the horizon and allowed practices, such as; installing electric batteries to vehicles and crossing milestones that improved energy density, safety, power, lifetime duration, and cost of the vehicles industry [22]. PMSM has a mass and volume that are comparative to its torque. A PMSM can be used for small vehicle applications that require smaller motors; thus, more suitable size magnets are used. Such application would greatly reduce the negative impact caused by combustion vehicles on the environment [23]. The main disadvantage that occurs due to replacing ICE engines with electrical batteries is mining for the metals that are required to create an electrical battery. The process of mining may cause negative impact on the environment. Mining for such metals reduces the air quality in the surrounding area, in addition to exposing the miners to different type of radiations and aerial particles that negatively affects their general health [24].

2.4.2 Social aspects

It is common that fuel energized engines are loud which makes electrical engines a better alternative, especially in areas with high populations. Also, electric vehicles are charged, which means the source of power is accessible easier for users than other sources like petrol/gas. Furthermore, ICE engines tend to emit carbon monoxide which is a poisonous gas to human beings. By replacing the ICE with electrical engines; the carbon foot print of individuals becomes very minimal, hence, air pollution is reduced, providing healthier environment to occupants in the surrounding areas. In terms of safety, malfunctions in ICE engines can cause fire breakouts in the vehicle. On the other hand, electric engines have smarter systems that make them safer for the individual. Reliability and safety become crucial when the PMSM drives are utilized in high performance applications, so safety measures must be considered when designing the machine.

2.4.3 Economical aspects

Electricity is considered inexpensive compared to the regular combusting fuels. The overall efficiency and reduced carbon foot print that are gained by using electric vehicles result in reduction of operating cost over the lifetime of the vehicle [24]. The price of the magnets, depending on its size, affects the price of the generator. Therefore, it is crucial to keep in mind the economical aspects while designing and constructing permanent magnet generators to reach a satisfactory ratio and efficiency [25]. China controls the extraction and production of electrical generators' materials. This causes dependency on the Chinese mines, which increases the demand on the materials. In 2018, China had a growth of 11% when it comes to NdFeB permanent magnets exports. China exported NdFeB to approximately 104 countries which increased the value of its exports by 3%, raising it from US$49.14 per kilogram to US$50.40 per kilogram [26].

2.5 Ethical aspect

Rare earth magnets and materials used in electrical engines cause an ethical and environmental threat. The major ethical concern comes from the overharvesting of materials at a high rate which leaves the future generations at risk when it comes to sustainable supplies [27]. The materials can be light or heavy earth materials. Permanent magnets include Nd and B light rare-earth materials. Although the price of materials is reduced compared to the previous peak, there are still possibilities for the price to rise again, in addition to various challenges related to sustainability. Reducing or eliminating the use of rare materials is recommended for future electric motor design. Solutions would be following designs that reduce or eliminate the usage of such rare materials in constructing electric motors, following designs that reduce or eliminate the usage of rare earth permanent magnets, and eliminating the usage of permanent magnets in electric motors. In order to overcome the ethical issues, latest motor topologies are classified into three types [28]:

- Designs with reduction in rare-earth materials
- Designs without rare-earth materials
- Designs without using permanent magnets

3

Methodology

Two identical axial flux permanent magnet machines with 4kW rated power are used for calculating the following analysis. There are three main stages to determine the laboratory readings in comparison with the readings obtained from the FEM simulation. The first step is to dismantle one of the two available AFM's in order to obtain the parameter specifications for further studies. The second stage presents the experimental setup done for running the steady-state tests of the axial flux PMSM in the laboratory, which include both load and open-circuit tests. The last step is modelling the machine using the Ansys Maxwell software, where the parameters from the first step are used in the modelling procedure.

3.1 Machine dismantling

Since the specifications of the machine were not provided with the delivered model, the dismantling of the AFM is performed to verify the main parameters in order to identify the topology used for modelling. In addition, the number of windings, the number of permanent magnets, the shape of the slots, and the material of the components are also determined. The dismantling of the machine was performed at Volvo Cars Company with the assistance of professionals, where the casing of the machine was first removed, then the stator and rotor parts were separated, after that the stator was cut to three different main sections to study the shape and type of the windings.

When the removal of the machine casing was completed, the type of the used machine is approved to be a non-salient inner rotor dual stator AFPMSM as can be seen in Figure 3.1.

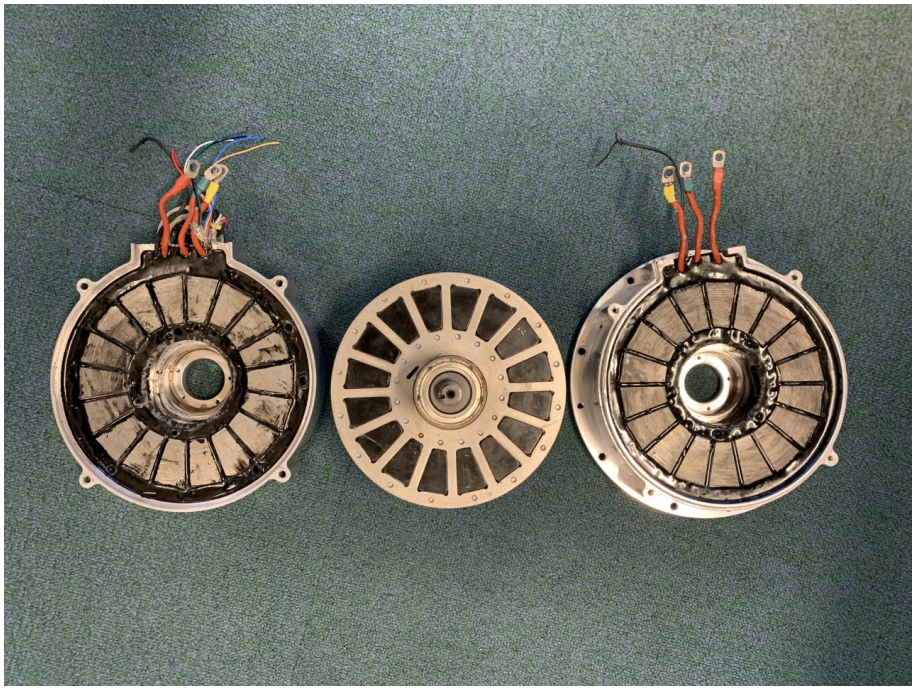

Figure 3.1: The main parts of the machine

The parametric measurements taken from the stator and rotor dismantled parts are given in Table 3.1 and Table 3.2.

Table 3.1: Stator parametric measurements

Description	Value
Number of slots	18
Core outer diameter	167.5mm
Core inner diameter	94mm
Thickness of the stator	30mm

Table 3.2: Rotor Parametric Measurements

Description	Value
Number of Poles	16
Core outer diameter	186.2mm
Core inner diameter	38mm
Thickness of the rotor	3.3mm

As seen in Figure 3.2 lines A, B, and C show the locations where the machine was cut. Line A, which cut the machine at the middle, assists in determining the placement and the connection of the windings. While the cut at Line B shows more accurate measurements of the dimensions of the stator slots. To obtain more information on the type of windings, the cut at Line C is utilised.

(a) 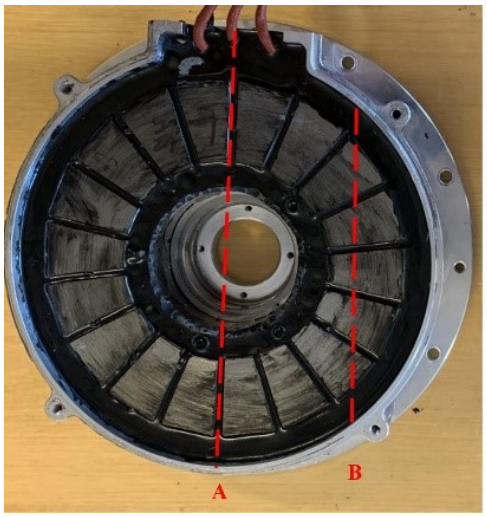

(b) 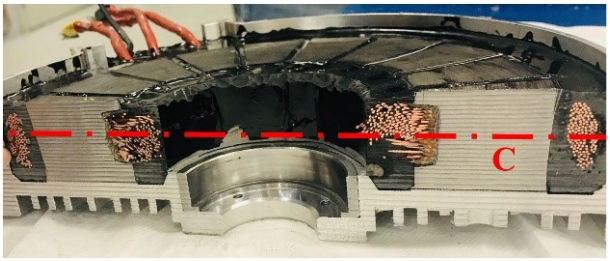

Figure 3.2: a)AFM with cut lines A and B b) AFM with cut line C

Therefore, Figure 3.3 shows the plan view of the machine after the three cuts were made. Following this procedure, the type of the used winding structure is determined to be a V-shaped Fractional-Slot Concentrated Winding (FSCW).

(a) 
(b) 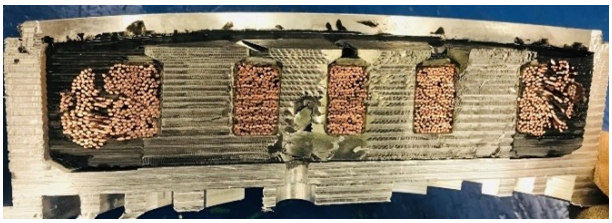

Figure 3.3: a) AFM after the cuts A and C are made b) AFM after cut B is made

From Figure 3.3-b, it is observed that the coils are double layered in each stator; and the number of copper strands in each layer is approximately counted as 120.

Additionally, in Figure 3.4, the number of parallel strands are found as 12 per phase; thus the number of conductors is counted as $120/12 = 10$ in each coil. In Table 3.3, the windings specifications are presented.

Table 3.3: Coil Parametric measurements

Description	Value
Outer diameter of the coil	173.5mm
Inner diameter of the coil	94mm
Thickness of the coil	30mm
Number of parallel strands	12
Number of copper strands per layer	120
Number of conductors	10
Number of winding layers	2
length of the ring	5
Height of the ring	14
Deviation angle	15
Coil material	Copper

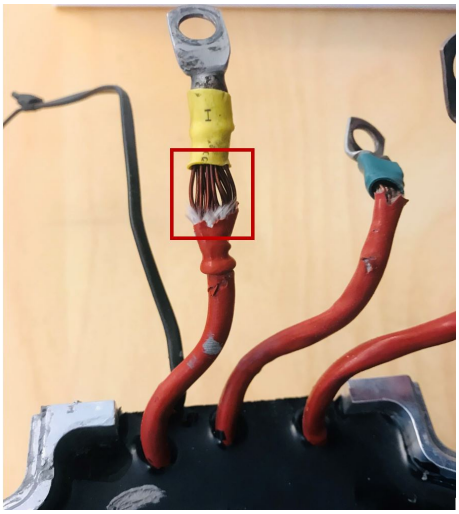

Figure 3.4: Number of parallel strands per phase

For the slots measurements, the following Figure 3.5 is obtained from Ansys software to illustrate the dimensions of the slots generated in 3.4.

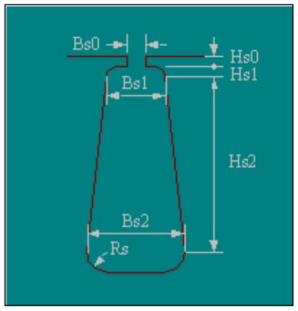

Figure 3.5: Dimensions of the slot

Table 3.4: Measurements of the slots

Name	Value	Description
Slot type	3	
Hs0	3mm	Slot Opening height
Hs1	3mm	Slot wedge height
Hs2	18mm	Slot body height
Bs0	4mm	Slot opening width
Bs1	12mm	Slot wedge maximum width
Bs2	12mm	Slot body bottom width
Rs	0.2	Slot body bottom fillet

The shaft on the FEM model is designed differently from the shaft in the actual model. The only difference in the dimensions is the thickness of the shaft; however, the diameter remains similar. The reason behind these measurements is to apply a more straightforward implementation of the shaft rotation with the rotor. These changes do not affect the output results of the simulation in comparison with the actual motor. The measurements of the shaft which are applied on Ansys software are presented in Table 3.5

Table 3.5: Shaft Parametric measurements

Description	Value
Diameter of the shaft	38mm
Thickness of the shaft	7mm

3.2 Experimental testing of the AFM

An experimental setup is carried out to test the performance of the AFM at different speed levels. A load and an open-circuit tests are performed to obtain the

measurement results used for comparison. Furthermore, the results obtained from the experiment will be used for validation purposes when compared with the FEM analysis.

The equipment of the experimental test includes a 144 V/110 A electric vehicle (EV) controller with a built-in inverter. The EV controller is managed using a CAN Analyzer tool to allow the communication between the digital device and the axial flux PMSM. In addition, a 4.5 kW DC machine is used as a load when testing the AFM for a full load test. To run the axial flux PMSM, a DC power supply of 300 V/20 A is used. While for operating the DC-machine, a power panel with a 400 V/20 A grid is used. The grid voltage is converted to ±440 V/±25 A using a thyristor converter. The control panel is used to adjust the input speed and input current of the DC machine within the thyristor converter panel. From the power panel, the inverter of the AFM is connected to the voltage sensors with a maximum value of ±650 V, and current sensors with a maximum value of ±35 A to analyse the phase voltages and phase currents. Figure 3.6 shows the connection diagram of the experimental setup.

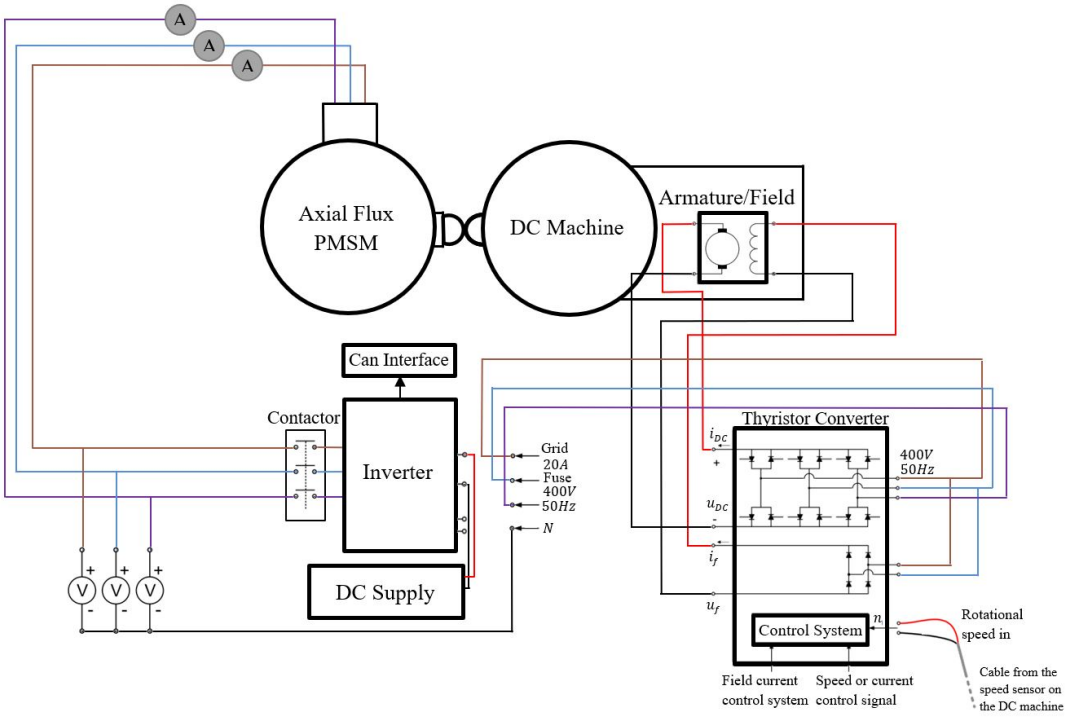

Figure 3.6: Connection diagram for the experimental setup of the AFM

During the open-circuit test, the inverter of the AFM is disconnected, and from the DC motor control panel, a speed reference is given to rotate the shaft of the AFM. As for the load test, the inverter is connected to the AFM, and by using the CAN Analyzer interface, torque is given to the AFM in order to start rotating. Additionally, the DC machine is used to drive the AFM, as shown in Figure 3.6. The thyristor converter control adjusts the speed alternately. This means that the AFM is now in torque control mode, and the DC machine is in speed control mode. By varying the speed, values of the armature current are selected accordingly, and the field current is set at 1.5 A. The LabVIEW software is used during the tests to measure the phase voltages, phase currents, torque, and ac power. Further detailed data of the AFM, EV controller, CAN Analyzer, stator resistance measurements, and current measurements are presented in the following.

3.2.1 Axial flux machine

This type of AFM is tested for electric vehicle applications. Since the AFM is commonly used for its high efficiency and reduced weight and size, it is considered an ideal option for an in-wheel direct drive system. The size of the experimented AFM used in this thesis is relatively smaller than the one used in electric vehicle applications, which suits the specifications of the available testing facility. The used AFM has an encoder mounted on the center of the machine as seen in Figure 3.7-a. The encoder cables are connected with the EV controller, where the temperature and the resolver signals are measured as shown in Figure 3.7-b. However, the temperature was not monitored in this experiment, and the resolver was not used. The parameters of the AFM are shown in Table 3.6, whereas the technical data is presented in A.1.

(a)

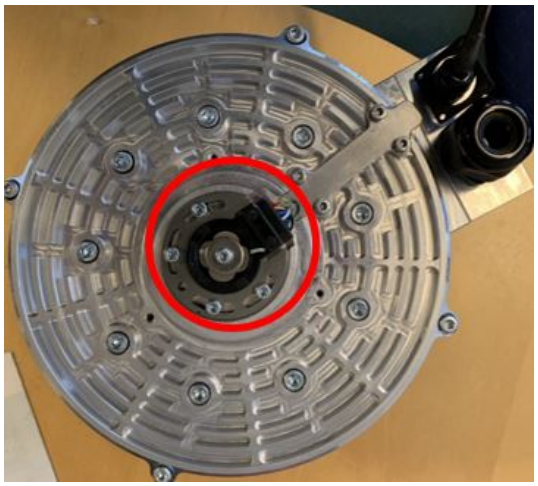

(b)

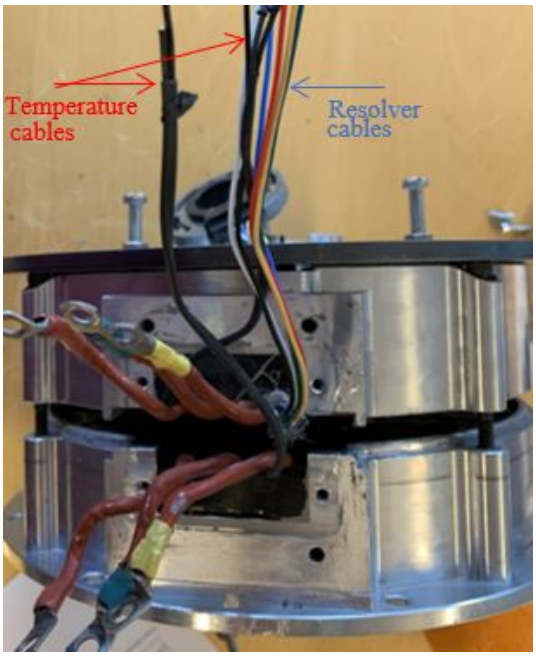

Figure 3.7: (a) Location of the mounted encoder around the center (b) Temperature and resolver cables

Table 3.6: Technical specifications of the AFM

Model: 4kW E-Motor (TZ165XFZH4096G)	
Description	Value
Voltage	$96V_{DC}$
Rated Power	4kW
Peak Power	8kW
Rated Speed	2000rpm
Maximum Speed	4000rpm
Rated Torque	19Nm
Peak Torque	50Nm
Cooling method	Natural air cooling

3.2.2 Electric vehicle controller

The chosen controller is intended for effective vehicle control of a three-phase AC asynchronous motor. The type of the control technique used in the EV controller is the field-oriented control (FOC), which modifies both the speed and torque of the AFM. In addition, the controller is provided with flexible functions to adjust the motor parameters and control the field weakening by using a CAN bus communication interface. For the controller to start operating, it is required to have a $\pm 12\,\mathrm{V}$ con-

nection with an additional DC power supply. The electronic characteristics, along with the wiring diagram, are shown in A.2.

3.2.3 CAN Analyzer

The type of communication interface used in this experiment is a USBCAN-II module with its associated software. The used EV controller is designed specifically with a CAN analyzer interface to acquire the measurements from the motor's electrical and mechanical characteristics during the operation. The analyzer contains a dual-channel intelligent CAN interface module with three pins at each of the channels, as seen in Figure 3.8. In Figure 3.8, the pins labeled as H and L present the signal cables, while the pins labeled as S and G present the shield cables. The switches R1 and R2 present the terminal resistance that is internally connected to pins H and L, respectively. Both CAN channels 1 and 2 are pinned with the controller connectors. When the connection between the PC and the EV controller is made, the software is used subsequently to start the AFM by controlling the torque and frequency input settings. A more detailed data sheet about the USBCAN interface is included in A.3.

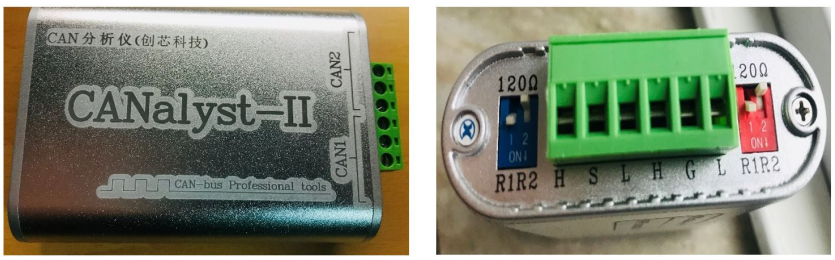

Figure 3.8: CAN Analyzer Interface

3.2.4 Stator resistance measurements

The stator resistance measurements were carried out in the laboratory. Figure 3.9 shows the terminal setup of the tested AFM, where the upper and lower 3-phase windings of the stators are shown. The chosen method of measuring the stator resistance is through connecting an Ammeter and a Voltmeter across two phases of either the upper or lower stator windings, as can be seen in Figure 3.10. The known

DC voltages are applied as an input of the DC supply source; hence the DC current is measured.

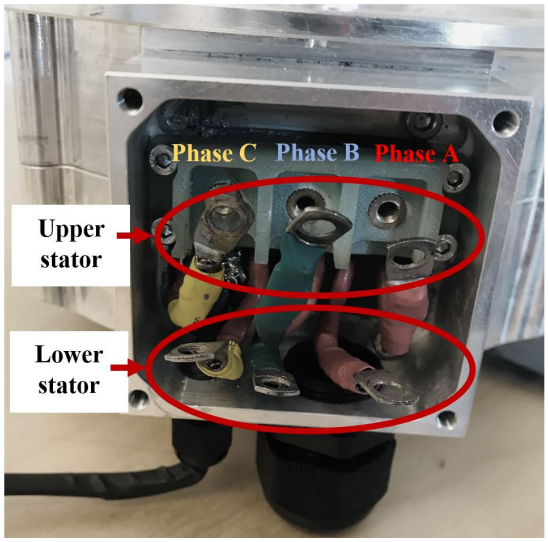

Figure 3.9: Star connection terminal of the AFPM showing the upper and lower 3-phase stator windings

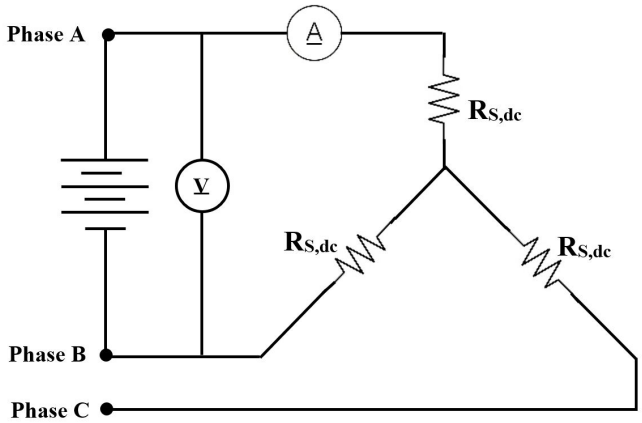

Figure 3.10: Stator resistance connection setup showing the connection of the DC voltage supply across two stator terminals

The measurements of the voltage and current across two phases are displayed in Table 3.7. Thus, the ratio of the average value of V_{dc} over I_{dc} are presented in Table 3.8.

Table 3.7: Voltage and current measurements between two stator terminals

Current (A)	Voltage (V) [PhaseA-PhaseB]	Voltage (V) [PhaseA-PhaseC]	Voltage (V) [PhaseB-PhaseC]
0.5	0.019	0.019	0.017
1.0	0.036	0.037	0.037
1.5	0.057	0.053	0.053
2.0	0.078	0.072	0.074
2.5	0.092	0.089	0.092
2.9	0.105	0.103	0.104

Table 3.8: Calculated ratio of $(\frac{V_{dc}}{I_{dc}})$

Current (A) $[I_{dc}]$	Average Voltage (V) $[V_{dc}]$	$\frac{V_{dc}}{I_{dc}}$
0.5	0.018	0.036
1.0	0.0367	0.0367
1.5	0.0543	0.0362
2.0	0.0746	0.0372
2.5	0.0913	0.03652
2.9	0.104	0.03586

Hence, the total average value of $\frac{V_{dc}}{I_{dc}}$ is 0.03641. The stator resistance for a star connection is measured as

$$R_{s,dc} = \frac{1}{2}\frac{V_{dc}}{I_{dc}} = \frac{0.03641}{2} = 0.0182\Omega \tag{3.1}$$

Thus, the stator resistance per phase for the experimented AFM is 0.0182Ω

3.2.5 Current measurements

Three current sensors of type LEM LA 50-S/SP1 modules are used in the laboratory testing setup. The current transducers are connected in a pre-assembled power board, where the measurements are viewed on the LabView program. A pre-created design on LabView is used to sample the output signal for the current of the machine. This type of current transducers has galvanic isolation between the primary and secondary circuits. The measured input current I_1 is proportional to the secondary

current I_2 that is produced by the current sensor. The output voltage is measured through the resistor where the current I_2 flows, as illustrated in Figure 3.11. The data sheet of the used current transducers can be viewed in A.4.

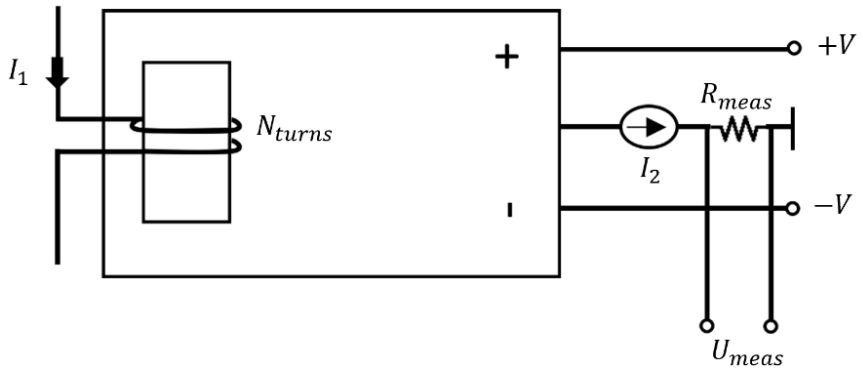

Figure 3.11: Current measurement setup

From Figure 3.11, the relation between the currents I_1 and I_2 is measured as

$$I_1 = \frac{N_s}{N_p} I_2 \tag{3.2}$$

where N_p is the number of turns, and N_s is 1:1000, which is the conversion ratio of the current transducer. The number of turns affects the measurement's level of accuracy, where a high number of turns leads to better readings accuracy. However, due to the choice of selecting a previous assembled connection in the lab, the number of turns was chosen to be 2 for a 35 A nominal current, and this results in a secondary current I_2 value of 70 mA. The voltage measured through the resistance is given as 5 V, thus the R_{meas} becomes

$$R_{meas} = \frac{U_{meas}}{I_2} = 71.4\Omega \tag{3.3}$$

A scaling factor is applied to the current and voltage transducers. The maximum current and voltage sensor's values are 35 A and 650 V, respectively. Thus, the measured current sensor values are multiplied by 35 A over 5 (the scaling factor), and the voltage sensors are multiplied with a DAQ voltage ratio of 650/5(scaling factor) at a full conversion card.

3.3 Finite element model implementation

The model measurements taken from section 3.1 are used to create a FEM model using the Ansys Maxwell 3D program. The modelling process will include specifications about the symmetry and boundary conditions, band implementation, air gap calculation, permanent magnets implementation, winding pattern, core materials, and losses and efficiency calculation.

3.3.1 Symmetry boundary conditions

By applying the values shown in Table 3.1 and Table 3.2, the whole geometry of the AFM is presented in Figure 3.12.

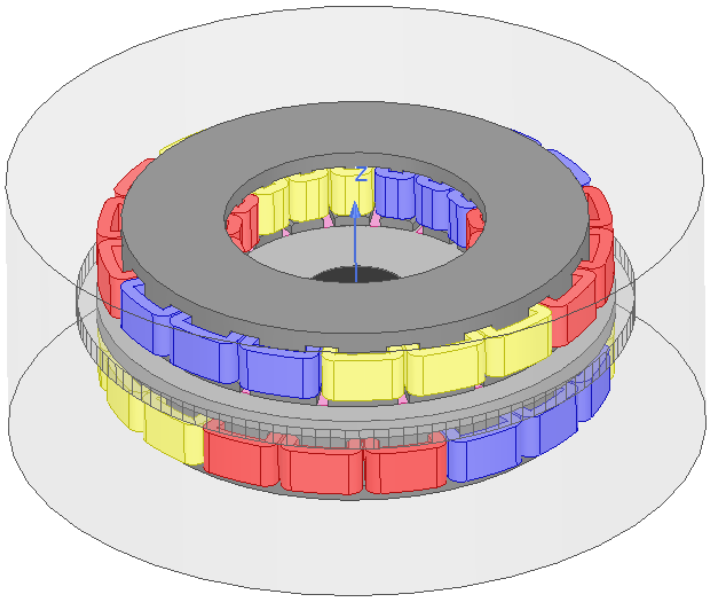

Figure 3.12: Full model of the AFM using Ansys Maxwell software

The full model analysis of the machine is used to verify the magnetic field direction. However, to reduce the simulation time, a quarter cut of the machine is simulated as in Figure 3.13.

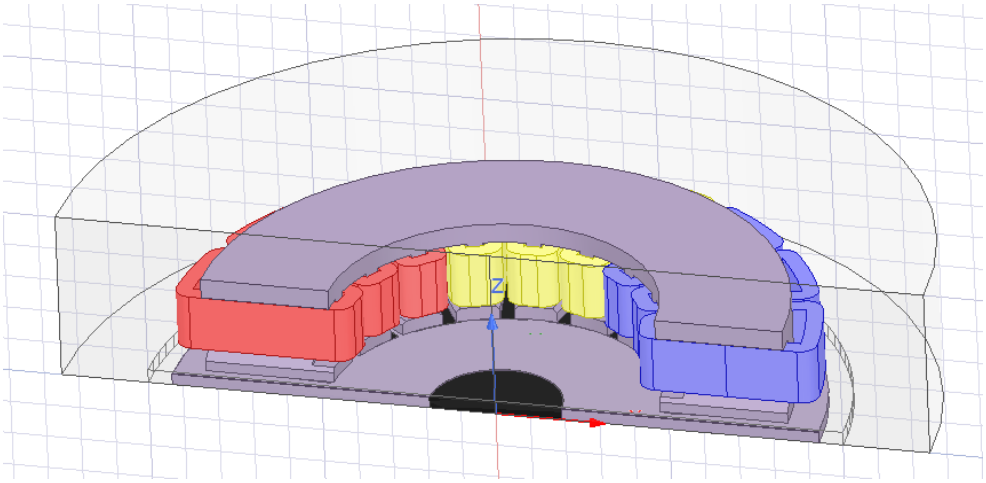

Figure 3.13: Quarter cut model of the AFM using Ansys Maxwell software

Thus, the boundary condition is defined accordingly for both planes in order to ensure symmetry. Due to the magnetic field caused by the magnet's behavior, the simulation is affected by the lower side of the selected quarter. Thus, to cover all parts in this simulation, a symmetry multiplication of two is added to the simulation settings. In the split xz-plane, the boundary is selected as a periodic boundary, also referred to as Master and Slave boundaries as shown in Figure 3.14 and Figure 3.15.

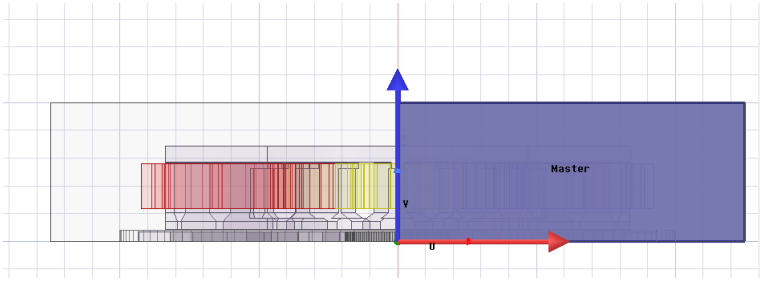

Figure 3.14: Master boundary

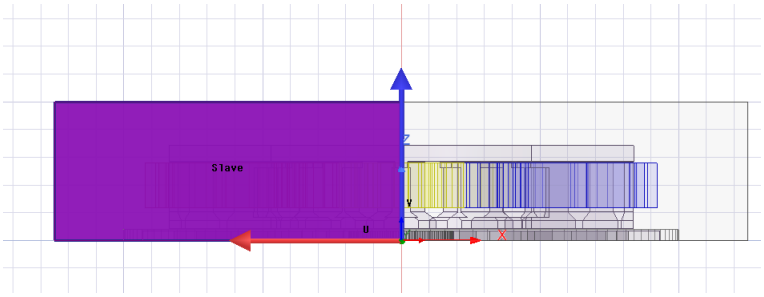

Figure 3.15: Slave boundary

This boundary is applied when both geometry surfaces of the Master and Slave have the same magnetic fields but different phase shifts [29]. Additionally, an even flux Symmetry boundary is added to the split in the xz-plane, where the machine's central point is now positioned at z=0 as seen in Figure 3.16.

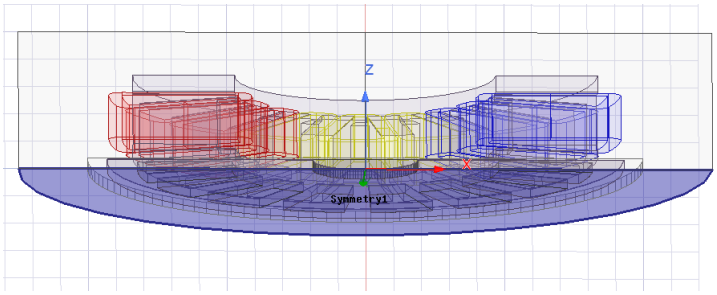

Figure 3.16: Symmetry boundary

The reason for using this boundary is to create a flux path that is perpendicular to the symmetry plane [29].

3.3.2 Band implementation

To define the rotation setup of the machine, a band needs to be created to cover the moving parts of the AFM, which should cover the entire volume of the rotor, shaft, and half of the air gap as seen in Figure 3.17. The measurements taken for the band are shown in Table 3.9. The rotation angle of the machine is chosen to be zero at t=0 when the phase A magnetic winding is aligned with the d-axis of the rotor. Thus, the maximum excitation of the stator and rotor is found at d-axis directing at 26.25 ° relative to the x-axis, as demonstrated in Figure 3.18.

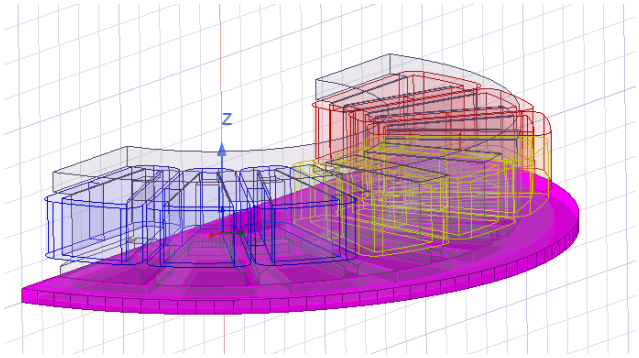

Figure 3.17: Band Implementation

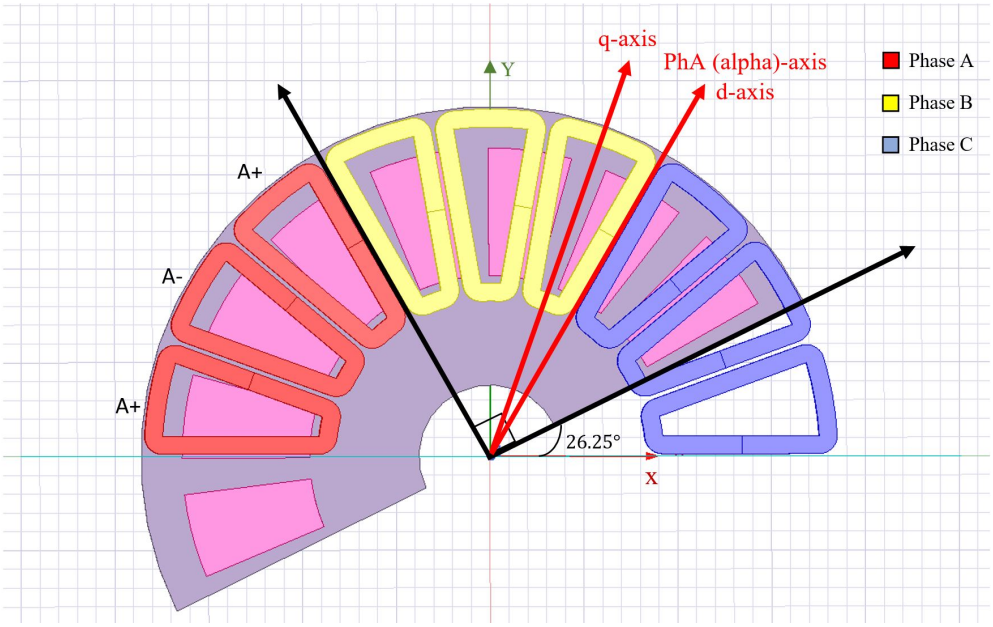

Figure 3.18: Angle of the initial position of the rotor

Table 3.9: Band measurements

Description	Value
Outer diameter of the band	173.5 mm
Band length	7 mm

3.3.3 Air gap calculation

Based on the measurements of the dismantled machine, the air gap is found by measuring the whole length of the machine then deducting the thickness of the stator and rotor as in

$$Airgap = Total\ Length\ of\ the\ machine - (Thickness\ of\ the\ stators + Thickness\ of\ the\ rotor) \tag{3.4}$$

$$Air\ gap = 68.5 - (30 \times 2 + 7) = 1.5mm \tag{3.5}$$

For both air gaps between the rotor and the double stator the value is then equal to $1.5/2 = 0.75$mm for each of the air gap lengths as shown in Figure 3.19.

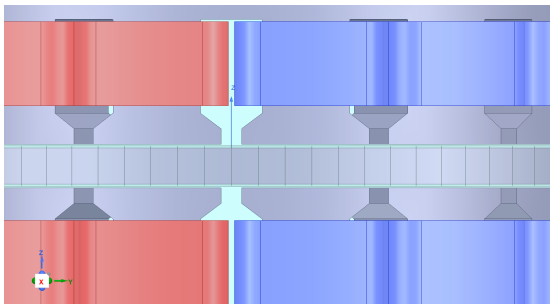

Figure 3.19: Air gap of the machine

3.3.4 Permanent magnets implementation

Based on the permanent magnets of the dismantled machine, the permanent magnet for the modelled AFM is chosen as a sintered Neodymium-Iron-Boron (NdFeB). This type of magnets is commonly known for its high magnetic performance. The AFM is modelled with magnets on the rotor in a 3D Cartesian coordinate system. Since the model of the AFM rotates in the axial direction, therefore the magnetization is aligned in the z-axis as seen in Figure 3.20.

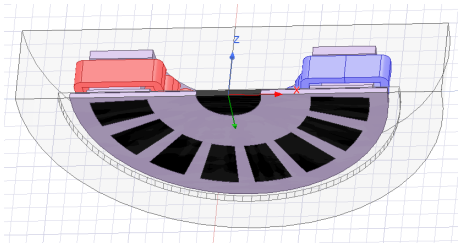

Figure 3.20: Magnets Implementation of the AFM

The chosen specifications of the NdFeB, regarding the relative permeability $\mu_{r,pm}$ and coercivity H_c, are 750 469 S/m and $-902.3\,\mathrm{kA/m}$, respectively. The values of the B-H curve are chosen as shown in Table 3.10.

Table 3.10: B-H curve specifications for NdFeB magnet

$H_{mag}[A/m]$	$B_{mag}[T]$
-902285	0
-451142	0.5912
0	1.1824

3.3.5 Winding pattern

The windings contain a respective number of turns of a conductor in reality; however, they are assumed to be solid in the model for simplicity. The method of exciting the windings in a 3D model is by applying a terminal inside each of the cross-sectional areas of the coils, as seen in Figure 3.21.

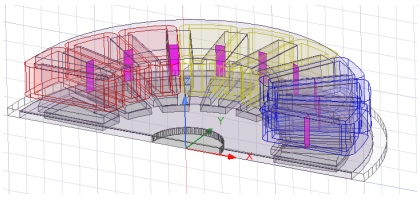

Figure 3.21: Excitation terminals Implementation of the AFM

The direction of positive and negative currents are perpendicular to the winding terminal, where the positive current direction implies that the current is flowing out of the plane, and the negative current direction implies that the current is flowing towards the plane. With having the terminal included in the model, adding several numbers of conductors in each of the terminals is feasible. The type of the winding, therefore, is chosen to be a 'Stranded' conductor, where the number of conductors per layer is assumed as 10. By choosing this option, the distribution of the current is even throughout the winding object. As mentioned in Section 3.1, the layout of the windings is found to be a fractional-slot double-layer 3-phase winding, and the way of modelling this layout is followed by [30] as shown in Figure 3.22.

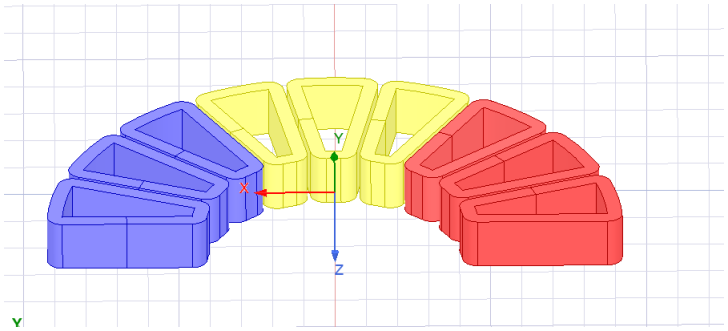

Figure 3.22: Winding Implementation of the AFM

3.3.6 Core materials and core losses

Since the core materials of the dismantled machine were not possible to identify, the steel alloy material selected for the rotor, stator, and shaft is chosen to be SURA 235-35A, which Surahammars Bruks AB manufactures. This type of steel is listed as one of the top materials based on EN 10106 standards [31]. As it is important for the AFM to produce a high torque density, the selection of material is made due to its magnetization behavior. The nonlinear BH-curve of SURA 235-35A material at 50 Hz frequency as presented in Figure 3.23, where all the measurements are taken from the data-sheet seen in A.5.

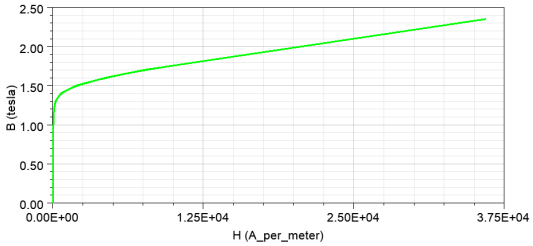

Figure 3.23: Nonlinear BH-curve of SURA 235-35A at 50 Hz

The core losses are calculated using the equation referred to in Section 2.3.9. In Ansys maxwell, the hysteresis losses, the excess losses , and the eddy current losses are determined from the data sheet inputs of the magnetic flux density versus the B-H curves of different frequencies, which is tested for [50, 100, 200, 400, 1000, 2500]Hz.

3.3.7 Losses and efficiency calculation

The instantaneous efficiency is determined to understand the characteristics of the AFM, where the copper losses (P_{cu}), core losses (P_{Fe}), and the AFM power (P_{AFM}) are defined in the FEM design. The calculation of the core losses is mentioned in section 3.3.6. To measure the copper losses, the stator resistance (R_s) is estimated by using the following relation

$$R_s = \frac{\rho L}{A} \tag{3.6}$$

where ρ is the resistivity and equal to $1.72 \times 10^{-8}\Omega m$, L is the length of the coil, and A is the cross-sectional area of the coil. The length is first measured for one strand as seen in Figure 3.24, which is calculated as 125mm and the thickness for one strand is found as 0.9mm. Therefore, for 1 strand of the coil, the area is computed as $\pi(0.45)^2 = 0.636mm$ and the resistance is found as $3.3805m\Omega$. Consequently, the resistance is calculated for 12 strands and 1 turn, and the value of the resistance is found as $0.282m\Omega$. Following by 10 turns and 12 strands, the value of resistance is found as $2.817m\Omega$. For a 3 phase winding of 18 slots, each phase contains 6 concentrated windings. Therefore, the estimated stator resistance calculated for 1 phase, 10 turns, and 12 strands, is found as 0.017Ω. To measure the AFM output power, the following equations is used

$$P_{AFM} = v_1 i_1 + v_2 i_2 + v_3 i_3 \tag{3.7}$$

The copper losses is found using the following

$$P_{Cu} = (I^2_{input,PhaseA} + I^2_{input,PhaseB} + I^2_{input,PhaseC}) R_s \tag{3.8}$$

The efficiency can be determined as

$$\eta = \frac{P_{out}}{P_{in}} 100\% = \frac{P_{AFM}}{P_{AFM} + P_{cu} + P_{Fe}} 100\% \tag{3.9}$$

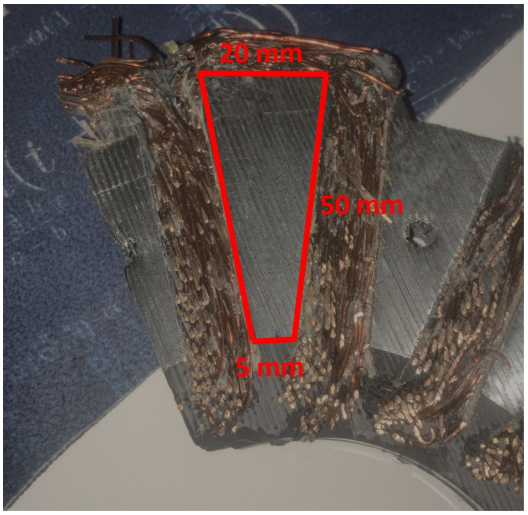

Figure 3.24: The measured values of the length for 1 strand of the winding

4

Case setup

A description of several cases, which are applied to the experimental setup and to the FEM simulation settings of the AFM, is presented in this chapter. The AFM is tested for two main tests: open-circuit test and load test. Three main speed references of 500, 1000 and 1500 rpm are chosen when testing the AFM. The same testing parameters are applied for both the experimental test and the finite element analysis.

4.1 Experimental testing cases

4.1.1 Open-circuit test

As the inverter of the AFM is disconnected for this test, the DC machine is in speed control mode, which drives the AFM to rotate. The speed references are varified from 500 rpm to 1500 rpm of the DC machine, and the measurements are recorded using the LabView software.

4.1.2 Load test

The AFM is tested for different DC input currents for the same speed levels of 500 rpm, 1000 rpm and 1500 rpm. A higher DC input current and a higher speed value were not tested due to the instability problem of the AFM on the testing rig, as well as to avoid overheating the machine.

4.2 Finite element modelling

4.2.1 Open-circuit test

The current excitation of the windings is kept to zero. The speed levels for the testing of the AFM is 500 rpm, 1000 rpm and 1500 rpm.

4.2.2 Load test

For the finite element analysis, the machine is simulated using an input of the amplitude values of the measured phase currents from the experimental test for the same speed levels of 500rpm, 1000rpm, and 1500rpm.

5

Analysis and discussion of results

The outcomes of both the laboratory test results and the FEM analysis results are presented in this chapter. The verification of the similarities for both tests is demonstrated in the open-circuit test and load test results section.

5.1 Open-circuit test results

A comparison between the measured results and simulated results of the open-circuit test is presented in this section. The results include a comparison between the induced voltages and flux linkages.

5.1.1 Induced voltage comparison

For the open-circuit case, the simulation is done for the speed levels of 500rpm, 1000rpm, and 1500rpm in order to get similar performance as the measured results in the lab. Fast Fourier Transform (FFT) is performed in order to find the fundamental values of the induced voltages. A comparison of the induced voltage results can be seen in Figure 5.1, and the data is shown in Table 5.1. As can be noticed from the Figure 5.1, the induced voltages are sinusoidal, and the amplitude of both the measured and simulated results are similar. The main noticeable difference in the outcomes is the time difference between both the measured and simulated results. This difference is due to the alteration of the sampling time during the motor testing in the lab.

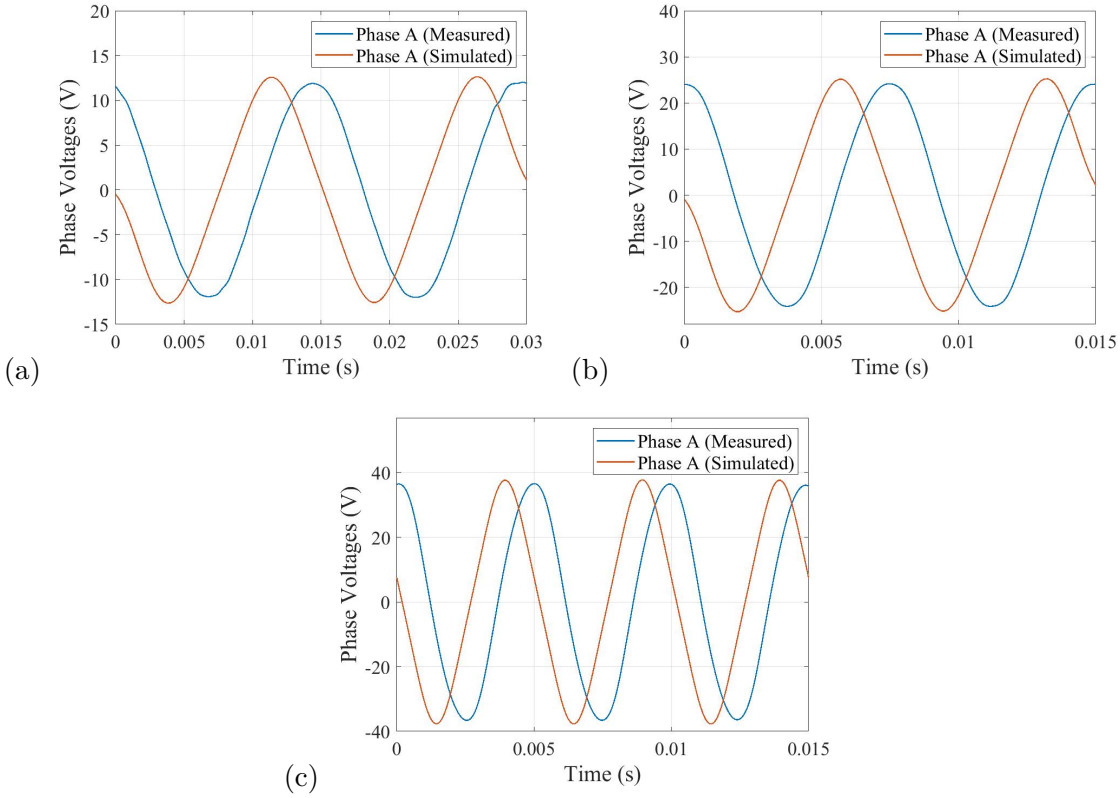

Figure 5.1: Induced voltage results of the measured and simulated tests for the cases of (a) 500rpm open-circuit, (b) 1000rpm open-circuit, and (c) 1500rpm open-circuit

Table 5.1: Induced voltage data of Figure 5.1

Speed	Induced voltage amplitude of the fundamental (V) [measured]	RMS voltage of the fundamental (V) [measured]	Induced voltage amplitude of the fundamental (V) [simulated]	RMS voltage of the fundamental (V) [simulated]
500rpm	$u_a = 12.0$ $u_b = 12.1$ $u_c = 12.1$	$u_{a,RMS} = 8.5$ $u_{b,RMS} = 8.6$ $u_{c,RMS} = 8.6$	$u_a = 12.1$ $u_b = 12.1$ $u_c = 12.1$	$u_{a,RMS} = 8.6$ $u_{b,RMS} = 8.6$ $u_{c,RMS} = 8.6$
1000rpm	$u_a = 24.2$ $u_b = 24.5$ $u_c = 24.4$	$u_{a,RMS} = 17.1$ $u_{b,RMS} = 17.3$ $u_{c,RMS} = 17.3$	$u_a = 24.1$ $u_b = 24.3$ $u_c = 24.3$	$u_{a,RMS} = 17.0$ $u_{b,RMS} = 17.2$ $u_{c,RMS} = 17.2$
1500rpm	$u_a = 36.4$ $u_b = 36.9$ $u_c = 36.6$	$u_{a,RMS} = 25.7$ $u_{b,RMS} = 26.1$ $u_{c,RMS} = 25.9$	$u_a = 37.6$ $u_b = 37.4$ $u_c = 37.1$	$u_{a,RMS} = 26.6$ $u_{b,RMS} = 26.4$ $u_{c,RMS} = 26.2$

5.1.2 Flux linkage comparison

A comparison between the measured flux linkage and the simulated flux linkage of the speed levels of 500rpm, 1000rpm, and 1500rpm is shown in Figure 5.2, and the peak values data for all speed levels are presented in Table 5.2. From Figure 5.2, It is noticeable that the peak values match for both the measured and simulated results. In addition, as mentioned in Section 3.3.2, it can be seen that the d-axis of the rotor is aligned with the peak of the A-axis at t=0.

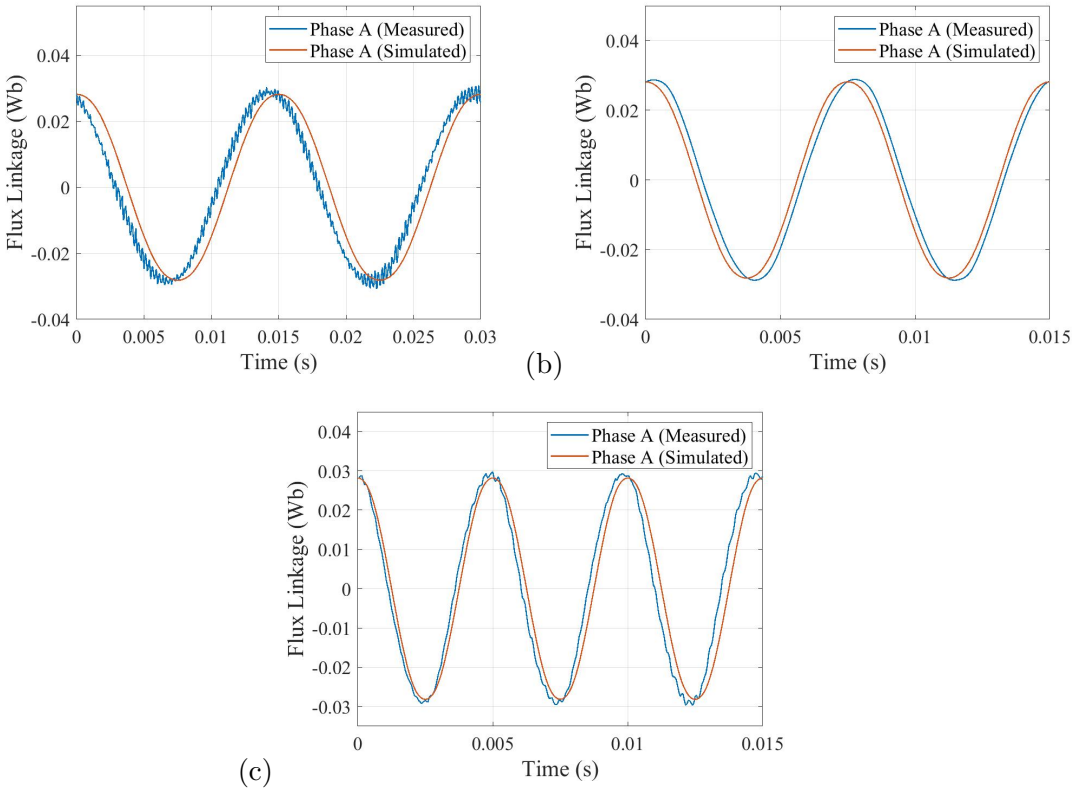

Figure 5.2: Flux linkage results of the measured and simulated tests for the cases of (a) 500rpm open-circuit,(b) 1000rpm open-circuit, and (c) 1500rpm open-circuit

Table 5.2: Flux linkage data of Figure 5.2

Speed	Peak value of the flux linkage (mWb) [measured results]	Peak value of the flux linkage (mWb) [simulated results]
500rpm	29	28
1000rpm	29	28
1500rpm	29	28

5.1.3 Torque

The expected result for the simulated torque in the open-circuit case is zero. Using the open-circuit measurements results, the torque from the AFM power and the torque from the DCM power are calculated as displayed in Table 5.4, where for both cases, core losses and mechanical losses are ignored. The calculated torque using the DC power is found using

$$T_{dc} = \frac{P_{dc} - P_{Cu,dc}}{\omega \frac{\pi}{30}} \tag{5.1}$$

where the DC copper losses is calculated using

$$P_{Cu,dc} = i_{dc}^2 R_a \tag{5.2}$$

where R_a is the armature resistance of the DC machine, and the value is given as 1.77Ω. Additionally, the calculated torque using the AFM power is found using

$$T_{AFM} = \frac{(P_{AFM,avg}) + (P_{Cu,AFM,avg})}{\omega \frac{\pi}{30}} \tag{5.3}$$

The results of the DC power and the DC copper losses for the speed levels of 500rpm, 1000rpm, and 1500rpm are shown in Table 5.3 .

Table 5.3: DC power and DC copper losses for the speed levels of 500rpm, 1000rpm, and 1500rpm

Speed	DC power P_{dc} (W)	DC copper losses $P_{Cu,dc}$ (W)
500rpm	40.7	2.0
1000rpm	90.4	2.5
1500rpm	145.2	2.8

Table 5.4: Calculated torque using the powers of the AFM and DC machine

Speed	Calculated torque using AFM power (Nm)	Calculated torque using DC power (Nm)
500rpm	0.005	0.7
1000rpm	-0.02	0.8
1500rpm	0.02	0.9

5.2 Load test results

In this section, the measured results and the simulated results are compared for the load case. The induced voltage, flux linkage, torque, angle difference, and losses between the measured and simulated results are presented.

5.2.1 Voltage comparison

For several inputs of DC values, the measured phase currents and phase voltages are taken for each of the speed levels of 500rpm, 1000rpm, and 1500rpm. The measured phase currents are used as an input current for the analysis. The data of the measured and simulated induced voltages and currents for the speed levels of 500rpm, 1000rpm, and 1500rpm is shown in Tables 5.5, 5.6, and 5.7, respectively.

Table 5.5: Induced voltage data of the measured and simulated results for the load case of 500rpm

Input DC current (A) [measured]	Phase current amplitude of the fundamental (A) [measured]	Phase voltages amplitude of the fundamental (V) [measured]	RMS voltages of the fundamental (V) [measured]	Input current amplitude of the fundamental (A) [simulated]	Phase voltage amplitude of the fundamental (V) [simulated]	RMS voltages of the fundamental (V) [simulated]
1.3	i_1= 7.5 i_2= 7.0 i_3= 7.3	u_1= 12.3 u_2= 12.5 u_3= 12.3	$u_{1,RMS}$= 8.7 $u_{2,RMS}$= 8.8 $u_{3,RMS}$= 8.7	7	u_1 = 12.3 u_2= 12.4 u_3= 12.4	$u_{1,RMS}$= 8.7 $u_{2,RMS}$= 8.8 $u_{3,RMS}$= 8.8
3.1	i_1= 15.3 i_2= 14.8 i_3= 14.9	u_1= 12.4 u_2= 12.0 u_3= 12.0	$u_{1,RMS}$= 8.8 $u_{2,RMS}$= 8.5 $u_{3,RMS}$= 8.5	15	u_1 = 12.6 u_2= 12.7 u_3= 12.7	$u_{1,RMS}$= 8.9 $u_{2,RMS}$= 9.0 $u_{3,RMS}$= 9.0
4.6	i_1= 21.2 i_2= 21.4 i_3= 21.6	u_1= 12.1 u_2= 13.0 u_3= 12.2	$u_{1,RMS}$= 8.6 $u_{2,RMS}$= 9.2 $u_{3,RMS}$= 8.6	22	u_1 = 12.9 u_2= 13.0 u_3=12.9	$u_{1,RMS}$= 9.1 $u_{2,RMS}$= 9.2 $u_{3,RMS}$= 9.1
6.5	i_1= 29.8 i_2= 29.2 i_3= 29.1	u_1= 12.3 u_2= 13.2 u_3= 12.4	$u_{1,RMS}$= 8.7 $u_{2,RMS}$= 9.3 $u_{3,RMS}$= 8.8	29	u_1 = 13.3 u_2= 13.4 u_3=13.3	$u_{1,RMS}$= 9.4 $u_{2,RMS}$= 9.5 $u_{3,RMS}$= 9.4
8.1	i_1= 36.4 i_2= 35.8 i_3= 35.6	u_1= 13.1 u_2= 13.1 u_3= 13.1	$u_{1,RMS}$= 9.3 $u_{2,RMS}$= 9.3 $u_{3,RMS}$= 9.3	36	u_1 = 13.7 u_2= 13.8 u_3=13.7	$u_{1,RMS}$= 9.7 $u_{2,RMS}$= 9.8 $u_{3,RMS}$= 9.7
10.0	i_1= 44.3 i_2= 43.7 i_3= 43.7	u_1= 14.1 u_2= 14.4 u_3= 13.5	$u_{1,RMS}$= 10.0 $u_{2,RMS}$= 10.2 $u_{3,RMS}$= 9.6	44	u_1 = 14.1 u_2= 14.2 u_3= 14.2	$u_{1,RMS}$= 10.0 $u_{2,RMS}$= 10.0 $u_{3,RMS}$= 10.0

Table 5.6: Induced voltage data of the measured and simulated results for the load case of 1000rpm

Input DC current (A) [measured]	Phase current amplitude of the fundamental (A) [measured]	Phase voltages amplitude of the fundamental (V) [measured]	RMS voltages of the fundamental (V) [measured]	Input current amplitude of the fundamental (A) [simulated]	Phase voltage amplitude of the fundamental (V) [simulated]	RMS voltages of the fundamental (V) [simulated]
1.0	i_1= 7.1 i_2= 6.0 i_3= 6.5	u_1= 23.3 u_2= 24.0 u_3= 24.1	$u_{1,RMS}$= 16.5 $u_{2,RMS}$= 17.0 $u_{3,RMS}$= 17.0	7	u_1 = 24.5 u_2= 24.6 u_3= 24.6	$u_{1,RMS}$= 17.3 $u_{2,RMS}$= 17.4 $u_{3,RMS}$= 17.4
2.9	i_1= 15.3 i_2= 14.0 i_3= 14.0	u_1= 24.0 u_2= 25.0 u_3= 24.1	$u_{1,RMS}$= 17.0 $u_{2,RMS}$= 17.7 $u_{3,RMS}$= 17.0	14	u_1 = 25.0 u_2 = 25.0 u_3= 24.9	$u_{1,RMS}$= 17.7 $u_{2,RMS}$= 17.7 $u_{3,RMS}$= 17.6
4.5	i_1= 21.9 i_2= 21.0 i_3= 20.2	u_1= 24.3 u_2= 24.5 u_3= 25.1	$u_{1,RMS}$= 17.2 $u_{2,RMS}$= 17.3 $u_{3,RMS}$= 17.7	21	u_1 = 25.4 u_2 = 25.6 u_3= 25.5	$u_{1,RMS}$= 18.0 $u_{2,RMS}$= 18.1 $u_{3,RMS}$= 18.0
6.2	i_1= 29.4 i_2= 27.7 i_3= 27.9	u_1= 24.1 u_2= 25.4 u_3= 24.8	$u_{1,RMS}$= 17.0 $u_{2,RMS}$= 18.0 $u_{3,RMS}$= 17.5	28	u_1 = 26.0 u_2 = 26.2 u_3 = 26.1	$u_{1,RMS}$= 18.4 $u_{2,RMS}$= 18.5 $u_{3,RMS}$= 18.5
7.9	i_1= 36.8 i_2= 35.1 i_3= 35.2	u_1= 24.8 u_2= 25.7 u_3= 24.7	$u_{1,RMS}$= 17.5 $u_{2,RMS}$= 18.2 $u_{3,RMS}$= 17.5	36	u_1 = 26.7 u_2 = 27.0 u_3 = 26.8	$u_{1,RMS}$= 18.9 $u_{2,RMS}$= 19.1 $u_{3,RMS}$= 20.0

Table 5.7: Induced voltage data of the measured and simulated results for the load case of 1500rpm

Input DC current (A) [measured]	Phase current amplitude of the fundamental (A) [measured]	Phase voltages amplitude of the fundamental (V) [measured]	RMS voltages of the fundamental (V) [measured]	Input current amplitude of the fundamental (A) [simulated]	Phase voltage amplitude of the fundamental (V) [simulated]	RMS voltages of the fundamental (V) [simulated]
1.1	i_1 = 7.9 i_2 = 6.0 i_3 = 7.3	u_1= 35.5 u_2= 32.7 u_3= 37.9	$u_{1,RMS}$= 25.1 $u_{2,RMS}$= 23.1 $u_{3,RMS}$= 26.8	7	u_1= 36.7 u_2= 37.0 u_3= 37.0	$u_{1,RMS}$= 26.0 $u_{2,RMS}$= 26.2 $u_{3,RMS}$= 26.2
2.8	i_1 = 15.6 i_2 = 13.4 i_3 = 14.	u_1= 35.5 u_2= 32.8 u_3= 39.1	$u_{1,RMS}$= 25.1 $u_{2,RMS}$= 23.2 $u_{3,RMS}$= 27.6	15	u_1= 37.2 u_2= 37.6 u_3= 37.5	$u_{1,RMS}$= 26.3 $u_{2,RMS}$= 26.6 $u_{3,RMS}$= 26.5
4.5	i_1 = 22.2 i_2 = 21.3 i_3 = 21.7	u_1= 36.0 u_2= 32.2 u_3= 39.7	$u_{1,RMS}$= 25.5 $u_{2,RMS}$= 22.8 $u_{3,RMS}$= 28.1	22	u_1= 37.9 u_2= 38.3 u_3= 38.1	$u_{1,RMS}$= 26.8 $u_{2,RMS}$= 27.1 $u_{3,RMS}$= 26.9
6.7	i_1 = 30.2 i_2= 27.3 i_3 = 28.6	u_1= 35.2 u_2= 36.4 u_3= 37.4	$u_{1,RMS}$= 24.9 $u_{2,RMS}$= 25.7 $u_{3,RMS}$= 26.4	29	u_1= 40.0 u_2= 39.1 u_3= 39.1	$u_{1,RMS}$= 28.3 $u_{2,RMS}$= 27.6 $u_{3,RMS}$= 27.6

In Figure 5.3, selected cases of the measured and simulated voltages versus the measured and simulated currents of all speed levels are displayed. Additionally, a comparison between the measured and simulated induced voltages for three selected input current values of the speed levels of 500rpm, 1000rpm, and 1500rpm is presented in Figure 5.4. It can be noticed from Figures 5.3 and 5.4 that after using a lowpass filter which resulted in reducing the noise, the measured induced voltage signals are still distorted. The distortion is expected to appear as shown due to the use of measuring equipment in the lab. Additionally, these measuring tools are not always reliable for providing ideal results. However, the overall behavior of both the measured and simulated induced voltages is similar, with an average peak value of 14V for 44A-500rpm, 25V for 36A-1000rpm, and 37V for 29A-1500rpm.

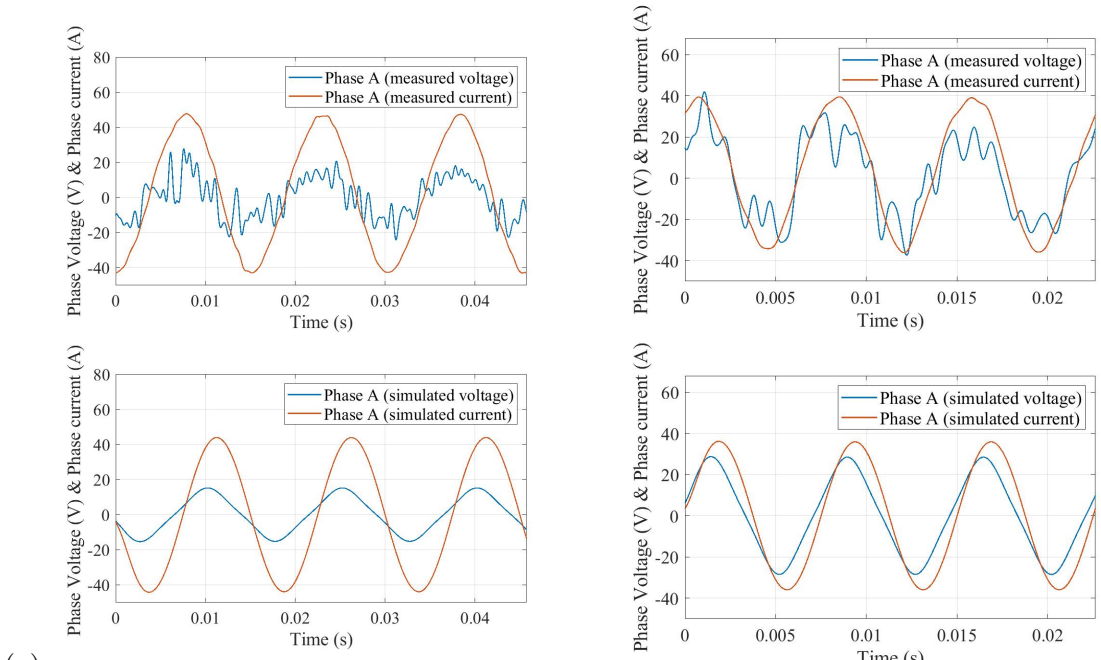

(a) (b)

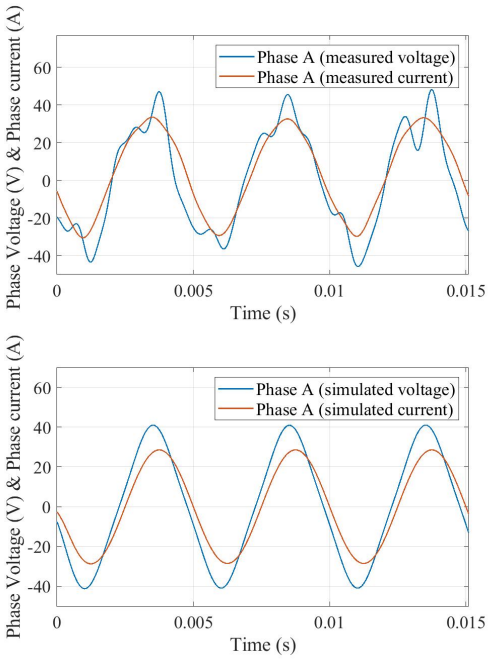

(c)

Figure 5.3: Voltage versus the input current of the measured and simulated results, (a) input current of 44A for 500rpm load case, (b) input current of 36A for 1000rpm load case, and (c) input current of 29A for 1500rpm load case

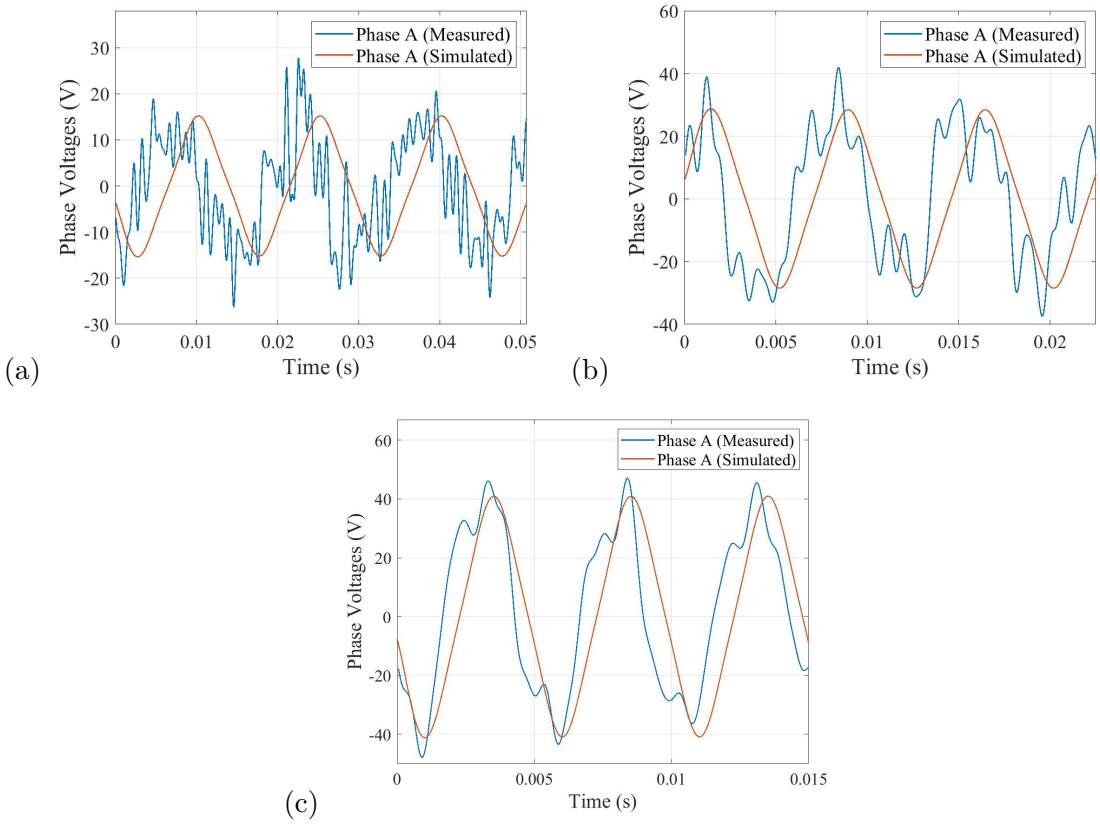

Figure 5.4: Voltage results of the measured and simulated tests, (a) input current of 44A for 500rpm load case, (b) input current of 36A for 1000rpm load case, and (c) input current of 29A for 1500rpm load case

5.2.2 Flux linkage comparison

For the same selected input currents of 44A, 36A, and 29A for the speed levels of 500, 1000, and 1500, respectively, the flux linkage of the measured and simulated results is displayed in Figure 5.5. The flux linkage results for the rest of the operating points are shown in Tables 5.8, 5.9, and 5.10. As can be seen from the figures, the behavior of both the measured and simulated flux linkage is as expected with similar peak values.

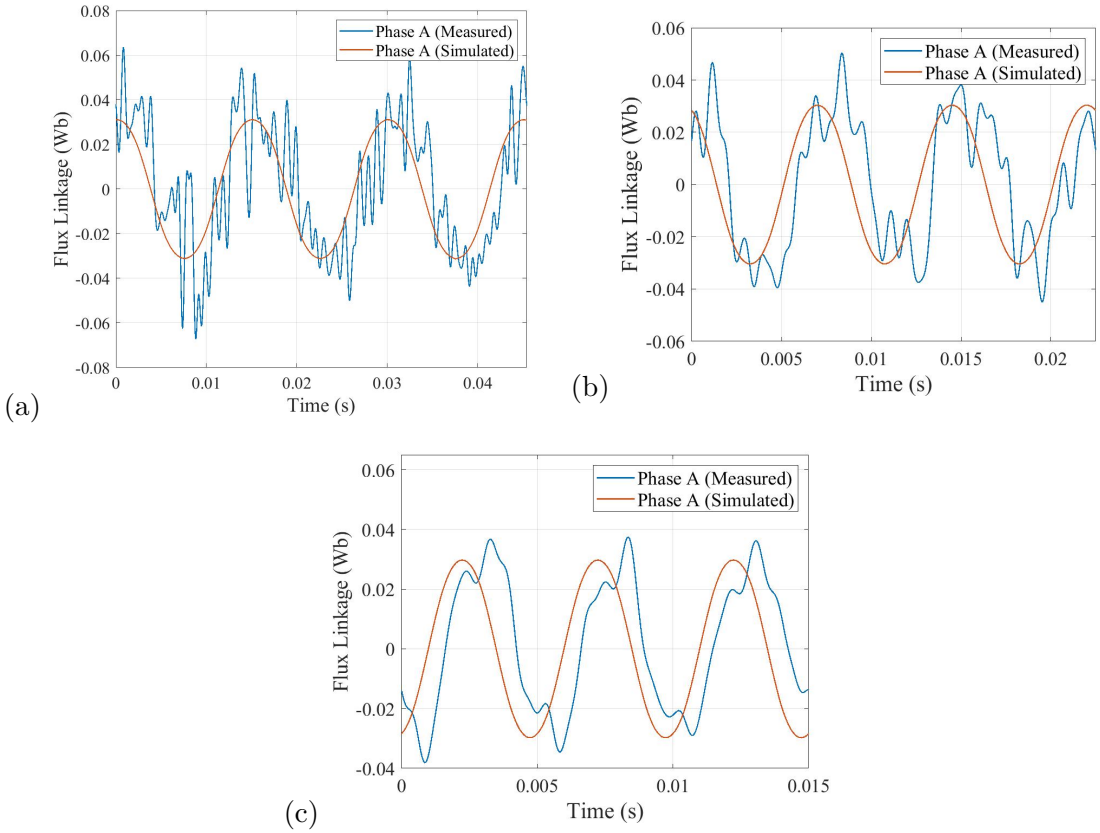

Figure 5.5: Flux linkage results of the measured and simulated tests for the load cases of (a) input current of 44A for 500rpm and (b) input current of 36A for 1000rpm (c)input current of 29A for 1500rpm

Table 5.8: Flux linkage data for the load case of 500rpm

Input current (A)	Amplitude value of the measured flux linkage (mWb)	Amplitude value of the simulated flux linkage (mWb)
7	37	28
15	39	29
21	40	29
29	42	30
36	45	31
44	42	31

Table 5.9: Flux linkage data for the load case of 1000rpm

Input current (A)	Average amplitude value of the measured flux linkage (mWb)	Average amplitude value of the simulated flux linkage (mWb)
7	34	28
14	35	29
21	36	29
28	35	31
36	38	31

Table 5.10: Flux linkage data for the load case of 1500rpm

Input current (A)	Average amplitude value of the measured flux linkage (mWb)	Average amplitude value of the simulated flux linkage (mWb)
7	32	29
15	33	30
22	33	30
29	36	30

5.2.3 Torque comparison

To present the torque ripples result, Figure 5.6 shows a simulated result for one selected case of 1500rpm and 29A input current. From Figure 5.6, it can be noticed that there are many ripples in the torque, and this is due to the structure of the permanent magnets. A possible way to limit these ripples is by applying some modifications to the rotor structure around the magnets or adding a second layer of magnets. The calculated torque using the AFM and DCM powers and the simulated air gap torque for the load test is presented in Figure 5.7, and the data for the torque results are shown in Tables 5.11, 5.12, and 5.13. As can be observed, the overall torque results are similar for both the calculated torque from the AFM and the simulated torque tests, but as can be noticed in Table 5.11, the values of the calculated torque are slightly higher than the simulated values for the input currents of 36A and 44A under the speed level of 500rpm. The reason behind the increase of torque values is possibly due to the measurement error.

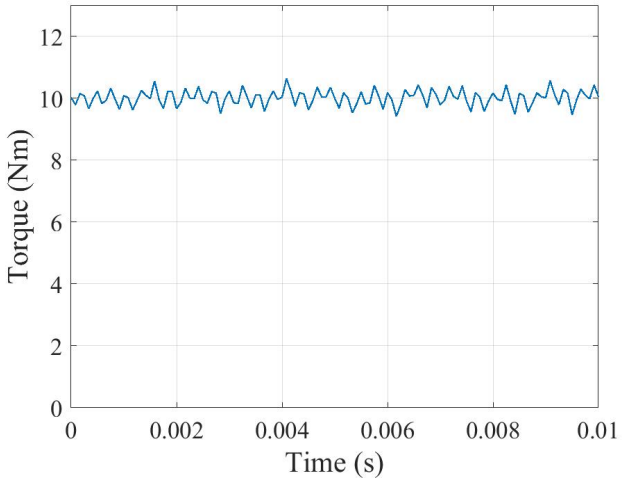

Figure 5.6: Torque ripples for the simulated case of 1500rpm and 29A input current

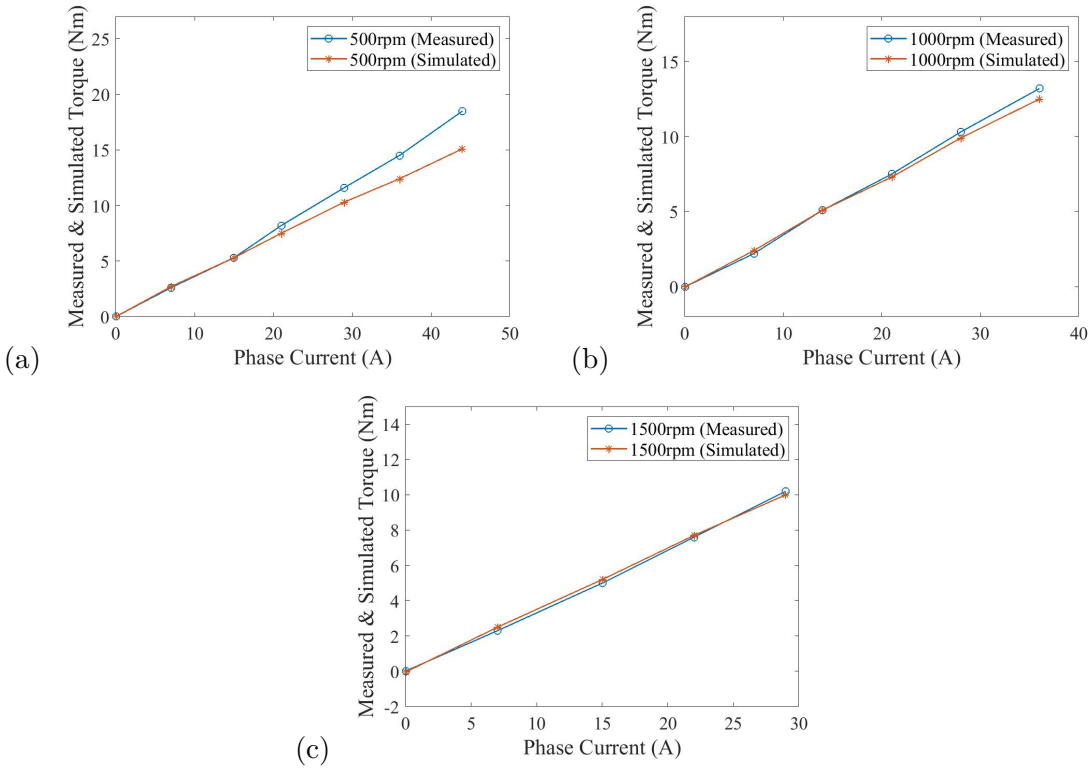

Figure 5.7: Calculated and simulated torque results for the load cases of (a) 500rpm (b) 1000rpm (c) 1500rpm

Table 5.11: Torque data for the load case of 500rpm

Input current (A)	Calculated torque using AFM power (Nm)	Calculated torque using DCM power (Nm)	Simulated torque (Nm)
7	2.6	1.4	2.7
15	5.3	2.9	5.3
21	8.2	3.9	7.5
29	11.6	4.6	10.3
36	14.5	4.9	12.4
44	18.5	4.9	15.1

Table 5.12: Torque data for the load case of 1000rpm

Input current (A)	Calculated torque using AFM power (Nm)	Calculated torque using DCM power (Nm)	Simulated torque (Nm)
7	2.2	1.3	2.4
14	5.1	3.5	5.1
21	7.5	5.3	7.3
28	10.3	6.8	9.9
36	13.2	8.2	12.5

Table 5.13: Torque data for the load case of 1500rpm

Input current (A)	Calculated torque using AFM power (Nm)	Calculated torque using DCM power (Nm)	Simulated torque (Nm)
7	2.3	1.5	2.5
15	5.0	3.7	5.2
22	7.6	5.6	7.7
29	10.2	7.6	10.0

5.2.4 Angle differences comparison

The angle difference between the voltage and current of the measured and simulated results is presented in Figure 5.8 and data are shown in Tables 5.14, 5.15, and 5.16. As can be noticed from the figure, there is a noticeable difference between the measured and simulated values. A possible reason is due to the change in sampling time, as mentioned earlier. Also, another reason is due to the use of a cheap Data Acquisition system (DAQ) when taking the measurements at the lab. This system has no Sample and Hold circuit, which leads the system to distribute the samples within a 50uS registration interval, instead of taking them all at the same time. Also, the simulated angle is the angle between the induced voltage and current, whereas the angle from the measurements is the angle between the terminal voltage

and current. Thus, a small difference is perhaps to be expected due to the referred Figure 2.7-c in section 2.3.2.

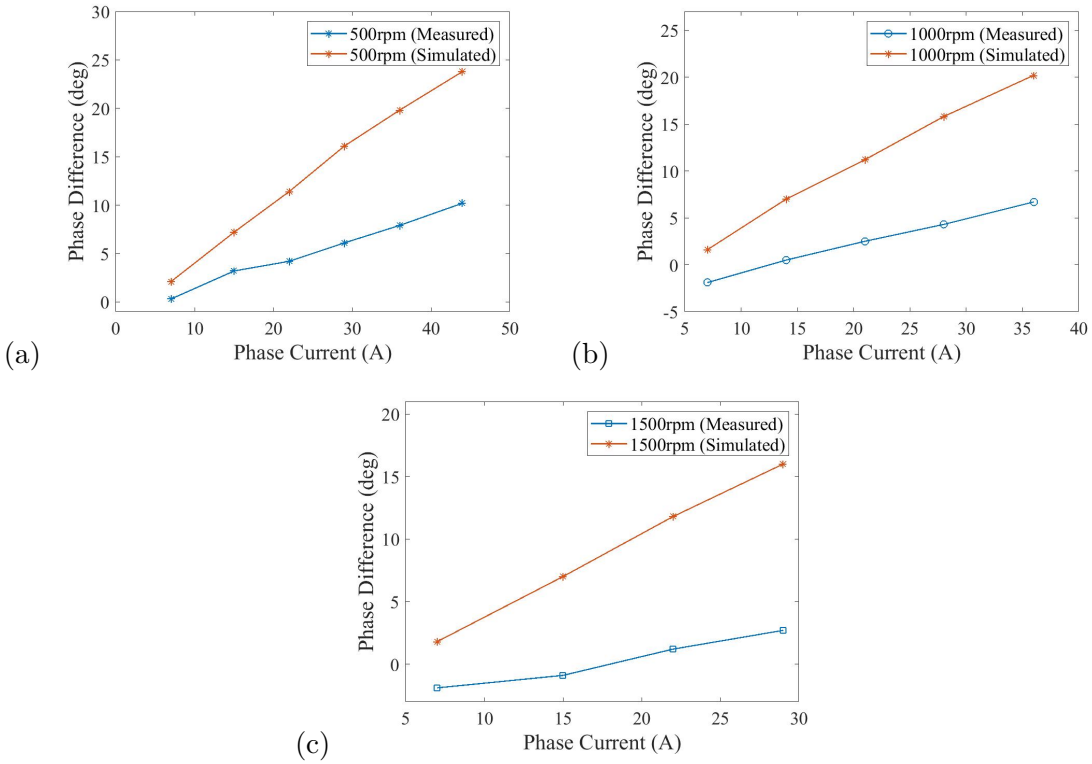

Figure 5.8: Measured and simulated angle differences results for the load cases of (a) 500rpm (b) 1000rpm (c) 1500rpm

Table 5.14: Angle difference data for the load case of 500rpm

Input current (A)	Average value of the measured angle difference $[\angle U - \angle I]$ (deg)	Average value of the simulated angle difference $[\angle U - \angle I]$ (deg)
7	0.3	2.1
15	3.2	7.2
22	4.2	11.4
29	6.1	16.1
36	7.9	19.8
44	10.2	23.8

Table 5.15: Angle difference data for the load case of 1000rpm

Input current (A)	Average value of the measured angle difference $[\angle U - \angle I]$ (deg)	Average value of the simulated angle difference $[\angle U - \angle I]$ (deg)
7	-1.9	1.6
14	0.5	7.0
21	2.5	11.2
28	4.3	15.8
36	6.7	20.2

Table 5.16: Angle difference data for the load case of 1500rpm

Input current (A)	Average value of the measured angle difference $[\angle U - \angle I]$ (deg)	Average value of the simulated angle difference $[\angle U - \angle I]$ (deg)
7	-1.9	1.8
15	-0.9	7.0
22	1.2	11.8
29	2.7	16.0

5.2.5 Losses and efficiency results

The calculated efficiency of the simulated AFM is shown in the contour plot as in Figure 5.9, where the iron losses and copper losses are added in order to calculate the efficiency. The simulation losses and efficiency data are presented in Tables 5.17, 5.18, and 5.19. It can be observed from Figure 5.9 that the highest efficiency value is mainly concentrated near high torque values. This problem can be improved when trying different core materials for the stator and rotor in order to minimize the core losses. The AFM power and iron losses for the measured results are shown in Tables 5.20, 5.21, and 5.22. Unfortunately, calculating the losses for the lab measurements is hard to do since the material and information of the iron used in the model are unknown. Also, the input power of the DC machine results in lower values than the output power, which is also due to the distortions introduced to the outcomes. And for this reason, the measured efficiency was in principle, not possible, to obtain.

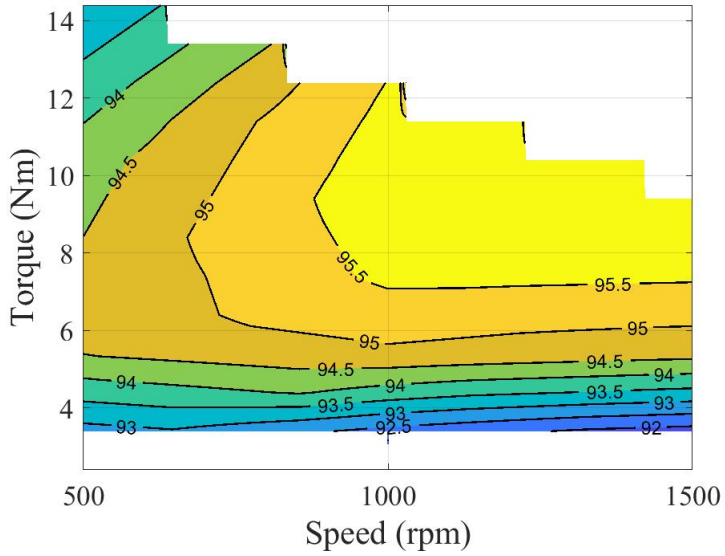

Figure 5.9: Calculated efficiency, where the copper losses and iron losses are considered

Table 5.17: Simulated loss data for the load case of 500rpm

Input current (A)	Copper losses, P_{Cu} (W)	Iron losses, P_{Fe} (W)	AFM power, P_{AFM} (W)	Efficiency $\frac{P_{AFM}}{P_{AFM}+P_{cu}+P_{Fe}} * 100\%$
7	1.4	10.1	135.6	92.2%
15	5.7	10.3	275.7	94.5%
21	11.7	10.6	393.7	94.6%
29	22.0	11.0	541.2	94.3%
36	33.1	11.4	661.1	93.7%
44	49.4	13.5	805.1	92.8%

Table 5.18: Simulated loss data for the load case of 1000rpm

Input current (A)	Copper losses, P_{Cu} (W)	Iron losses, P_{Fe} (W)	AFM power, P_{AFM} (W)	Efficiency $\frac{P_{AFM}}{P_{AFM}+P_{cu}+P_{Fe}} * 100\%$
7	1.1	23.2	241.8	90.9%
14	5.3	23.7	529.3	94.8%
21	11.3	24.3	772.6	95.6%
28	20.6	25.2	1045.7	95.8%
36	33.1	29.5	1323.1	95.5%

Table 5.19: Simulated loss data for the load case of 1500rpm

Input current (A)	Copper losses, P_{Cu} (W)	Iron losses, P_{Fe} (W)	AFM power, P_{AFM} (W)	Efficiency $\frac{P_{AFM}}{P_{AFM}+P_{cu}+P_{Fe}} * 100\%$
7	1.3	39.4	384.7	90.4%
15	5.4	40.3	805.1	94.6%
22	12.0	41.4	1198.5	95.7%
29	20.9	47.4	1579.5	95.9%

Table 5.20: Measured loss data for the load case of 500rpm

Input current (A)	Copper losses, P_{Cu} (W)	AFM power, P_{AFM} (W)
7	1.8	132.5
15	6.5	296.4
21	13.1	409.2
29	23.8	574.6
36	35.7	711.4
44	53.2	899.3

Table 5.21: Measured loss data for the load case of 1000rpm

Input current (A)	Copper losses, P_{Cu} (W)	AFM power, P_{AFM} (W)
7	1.6	230.9
14	6.3	526.8
21	13.5	770.9
28	22.8	1051.6
36	35.7	899.3

Table 5.22: Measured loss data for the load case of 1500rpm

Input current (A)	Copper losses, P_{Cu} (W)	AFM power, P_{AFM} (W)
7	2.1	365.2
15	6.8	772.1
22	14.6	1173.7
29	24.0	1572.8

6

Conclusion

6.1 Results from present work

The two identical AFM were used for the analysis: one machine was used for testing, and the second was used for dismantling in order to establish the geometry and then to design and validate the obtained simulated model. The outcomes of both the laboratory test and the simulation test were then compared, which is the main purpose of this thesis. The AFM was tested in the lab for three main speed levels and experimented on with open-circuit and load tests. Following the testing procedure, the AFM was simulated on a FEM software and was tested and validated for the same measuring outcomes to verify the efficiency and performance of the design.

Overall, the measured and simulated outcomes are similar, with few noted points. The phase difference between the voltage and current of the measured and simulated results was expected since the used measuring system was not reliable for testing; it needed further improvement. Even though there were few differences in the power angle due to the alteration of sampling time, the simulated voltages, currents, flux linkages, and torque have similar average values and matching behavior compared to the measurements taken from the laboratory test. Furthermore, the calculated efficiency of the simulated model showed promising results with an average efficiency value of 94%; however, the efficiency for the experimented AFM was not possible to obtain since some of the losses information was unknown. The percentage error calculation for the voltage and torque in both tests resulted in a percentage error that is less than 10%; however, for the flux linkage results, the percentage error was

less than 20%, which is due to the measurement error. The percentage error for the power angle difference was not calculated since the difference in values was too high due to the reasons mentioned in section 5.2.4.

6.2 Future work

Since the model has been validated, there is still room for improvement; various tests can be carried out for enhancing the measurements of the experimental test and design of the AFM. It would be interesting to test the simulated AFM machine by varying the parameters taken from the dismantled AFM machine in order to check for possibilities to improve the AFM in general applications.

Another recommended work regarding the simulated model is to try different material properties for the machine's core and magnets and check the performance in order to know which materials give desirable results with more minor losses. Another study is to improve the high-temperature performance of the machine at high speeds and higher current values would be concerning finding the thermal limit along with a cooling system of the simulated AFM.

Additionally, the AFM simulation can be tested for different winding setups, for example, single or double-layered, distributed, integral, fractional, air-cored, and iron-cored, and analyze the magnetization of the permanent magnets and its effect on the overall performance of the AFM. Also, it is interesting to study the performance of the simulated AFM regarding different topologies, such as single-sided, inner stator dual-sided rotor, and multi-disc AFM.

It would also be interesting to scale up the simulated AFM to vehicle size and check the performance of the machine in comparison to other types of electric motors that are mainly used in electric vehicle applications.

According to the recommendations related to the experimented AFM, adding a re-

solver in the test can improve the measurement results by giving an accurate value of the current angle.

Bibliography

[1] M. ALATALO, "Axial flux machine as a traction motor for electric and hybrid vehicles," *Technical report 2018: 1, Chalmers University of Technology Dep. Of Electrical Engineering*, 2019.

[2] A. Cavagnino, M. Lazzari, F. Profumo, and A. Tenconi, "A comparison between the axial flux and the radial flux structures for pm synchronous motors," *IEEE transactions on industry applications*, vol. 38, no. 6, pp. 1517–1524, 2002.

[3] A. Parviainen, M. Niemela, J. Pyrhonen, and J. Mantere, "Performance comparison between low-speed axial-flux and radial-flux permanent-magnet machines including mechanical constraints," in *IEEE International Conference on Electric Machines and Drives, 2005.* IEEE, 2005, pp. 1695–1702.

[4] A. H. Mohamed, A. Hemeida, H. Vansompel, and P. Sergeant, "Parametric studies for combined convective and conductive heat transfer for yasa axial flux permanent magnet synchronous machines," *Energies*, vol. 11, no. 11, p. 2983, 2018.

[5] J. F. Gieras, R.-J. Wang, and M. J. Kamper, *Axial flux permanent magnet brushless machines.* Springer Science & Business Media, 2008.

[6] R. L. Ficheux, F. Caricchi, F. Crescimbini, and O. Honorati, "Axial-flux permanent-magnet motor for direct-drive elevator systems without machine room," *IEEE Transactions on Industry Applications*, vol. 37, no. 6, pp. 1693–1701, 2001.

[7] E. Spooner, B. Chalmers, and M. El-Missiry, "A compact brushless dc machine," in *Electr Drives Symp EDS*, vol. 90, 1990, pp. 239–243.

[8] C. Du-Bar, "Design of an axial flux machine for an in-wheel motor application," *Chalmers Reproservice, Göteborg*, pp. 1–2, 2011.

[9] M. U. Lampérth, A. C. Malloy, A. Mlot, and M. Cordner, "Assessment of axial flux motor technology for hybrid powertrain integration," *World Electric Vehicle Journal*, vol. 7, no. 2, pp. 187–194, 2015.

[10] T. Woolmer and M. McCulloch, "Analysis of the yokeless and segmented armature machine," in *2007 IEEE International Electric Machines & Drives Conference*, vol. 1. IEEE, 2007, pp. 704–708.

[11] M. Alatalo, "Permanent magnet machines with air gap windings and integrated teeth windings," Ph.D. dissertation, Chalmers University of Technology, 1996.

[12] K. Xu, W. Chen, Y. Xu, M. Gao, and Z. He, "Vector control for pmsm," *Sensors / Transducers*, vol. 170, no. 5, p. 227, 2014.

[13] W. Soong and T. Miller, "Theoretical limitations to the field-weakening performance of the five classes of brushless synchronous ac motor drive," in *1993 Sixth International Conference on Electrical Machines and Drives (Conf. Publ. No. 376)*. IET, 1993, pp. 127–132.

[14] M. Li, "Flux-weakening control for permanent-magnet synchronous motors based on z-source inverters," 2014.

[15] N. Mohan, T. M. Undeland, and W. P. Robbins, *Power electronics: converters, applications, and design*. John wiley & sons, 2003.

[16] Ph.D. dissertation.

[17] S. Huang, M. Aydin, and T. A. Lipo, "Torque quality assessment and sizing optimization for surface mounted permanent magnet machines," in *Conference Record of the 2001 IEEE Industry Applications Conference. 36th IAS Annual Meeting (Cat. No. 01CH37248)*, vol. 3. IEEE, 2001, pp. 1603–1610.

[18] J. Wang, Z. P. Xia, and D. Howe, "Three-phase modular permanent magnet brushless machine for torque boosting on a downsized ice vehicle," *IEEE Transactions on Vehicular Technology*, vol. 54, no. 3, pp. 809–816, 2005.

[19] E. Furlani, "Permanent magnet and electromagnetical devices. rochester," 2001.

[20] J. Olivier, A. Bouwman, C. Van der Maas, and J. Berdowski, "Emission database for global atmospheric research (edgar)," *Environmental Monitoring and Assessment*, vol. 31, no. 1, pp. 93–106, 1994.

[21] D. Svechkarenko, A. Cosic, J. Soulard, and C. Sadarangani, "Transverse flux machines for sustainable development-road transportation and power generation," in *2007 7th International Conference on Power Electronics and Drive Systems*. IEEE, 2007, pp. 1108–1114.

[22] X. Zeng, M. Li, D. Abd El-Hady, W. Alshitari, A. S. Al-Bogami, J. Lu, and K. Amine, "Commercialization of lithium battery technologies for electric vehicles," *Advanced Energy Materials*, vol. 9, no. 27, p. 1900161, 2019.

[23] L. Sepulchre, M. Fadel, M. Pietrzak-David, and G. Porte, "Mtpv flux-weakening strategy for pmsm high speed drive," *IEEE Transactions on Industry Applications*, vol. 54, no. 6, pp. 6081–6089, 2018.

[24] S. Halder and X. Yang, "Extracting the maximum torque from a pmsm for a vehicular application by using different modulation techniques in the overmodulation region," 2019.

[25] N. Radwan/-Praglowska, "Impact of permanent magnets shape and arrangement for selected parameters in coreless axial flux generator," in *2018 International Symposium on Electrical Machines (SME)*. IEEE, 2018, pp. 1–6.

[26] "Adam's intelligence, "china's exports of ndfeb magnets increased 11% in 2018," February 2019. [Online]. Available: https://www.adamasintel.com/china-ndfeb-exports-increased-2018/

[27] K. Bourzac, "The rare-earth crisis," *Technology Review*, vol. 114, no. 3, pp. 58–63, 2011.

[28] E.-R. Ayman, "Toward a sustainable more electrified future: The role of electrical machines and drives," *IEEE Electrification Magazine*, vol. 7, no. 1, pp. 49–59, 2019.

[29] "user's guide – maxwell 3d," 2005. [Online]. Available: http://ansoft-maxwell.narod.ru/en/CompleteMaxwell3D_V11.pdf

[30] J. Wang, K. Atallah, Z.-Q. Zhu, and D. Howe, "Modular 3-phase permanent magnet brushless machines for in-wheel applications," in *2006 IEEE Vehicle Power and Propulsion Conference*. IEEE, 2006, pp. 1–6.

[31] K. Hruska, J. Laksar, and J. Sobra, "The determination of iron core loss characteristics of special electrical steel types," in *2018 18th International Conference*

on Mechatronics-Mechatronika (ME). IEEE, 2018, pp. 1–6.

A

Appendix 1

A.1 AFM Technical data

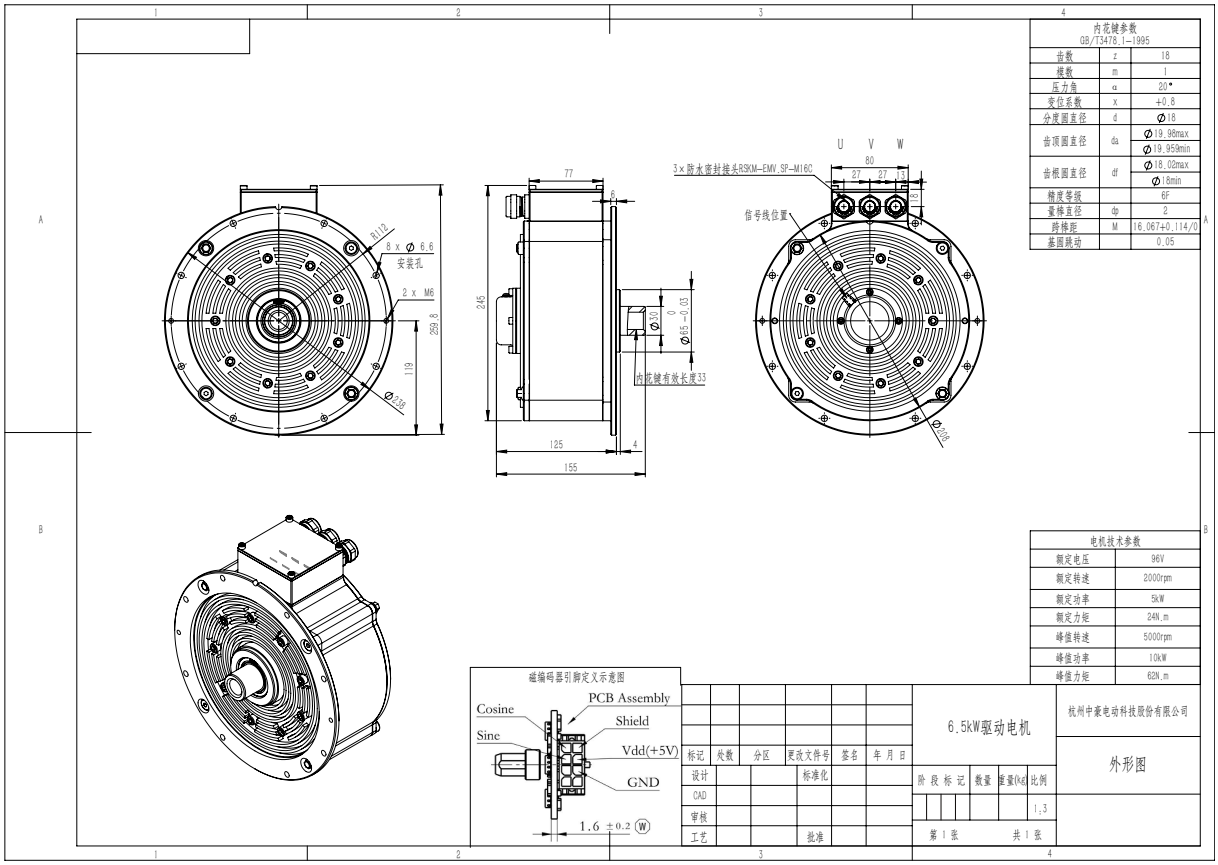

A.2 Electric vehicle controller specifications

D02 frame(IP67)

Key technical features (1)

Model	KTZ(KYS)07X*Z** KTZ(KYS)07X*F** KTZ(KYS)07X*S**	KTZ(KYS)11X*Z** KTZ(KYS)11X*F** KTZ(KYS)11X*S**	KTZ(KYS)14X*Z** KTZ(KYS)14X*F** KTZ(KYS)14X*S**	KTZ: Applicable for PMSM KYS: Applicable for ACIM X: Resolver Z: Natural cooling F: Fan cooling S: Water cooling
Electronic characteristics				
Auxiliary power voltage	6~16V DC			
Maximum auxiliary current	3A			
DC bus capacitor	12.21mF	8.14mF	8.14mF	
Rated battery voltage	60/72V DC	96/108V DC	120/144V DC	
Rated input current	Z: 130 A F: 230 A S: 250 A	Z: 120 A F: 230 A S: 230 A	Z: 110 A F: 180 A S: 230 A	Z: Natural cooling F: Fan cooling S: Water cooling
Input voltage range	40~90V	50~130V	70~180V	
Output voltage	54.5~85V	72.5~130	105V~170V	
Rated output current	Z: 120 A F: 230 A S: 250 A	Z: 120 A F: 200 A S: 230 A	Z: 110 A F: 150 A S: 220 A	Z: Natural cooling F: Fan cooling S: Water cooling
Peak input current	350A/450A/550A	350A/450A/550A	350A/450A/550A	Correspond to different numbers Mosfets
Ratedoutput current	350A/450A/550A	350A/450A/550A	300A/400A/500A	2 min
Rated output power	Z: 7.5kW F: 15 kW S: 17kW	Z: 11 kW F: 20 kW S: 23 kW	Z: 15 kW F: 20 kW S: 30 kW	
Peak output power	22kW/30kW/37kW	30kW/45kW/55kW	45kW/60kW/75kW	
Highest efficiency	≥98%			Rated
Output frequency	0.00~1000Hz			
Mechanical characteristics				
Dimensions	316*246.5*139(Natural cooling), 316*246.5*168(Fan cooling), 316.5*246.5*114(Water cooling)			See drawing
Installation dimensions	L*W-Φ=275*182-4φ10			
Weight	Z: 6.7 KG, F: 7.5 KG, S: 5.5 KG			
Screw torque of cover	M4*12，1.4Nm			

D02 frame(IP67)

Wiring diagram

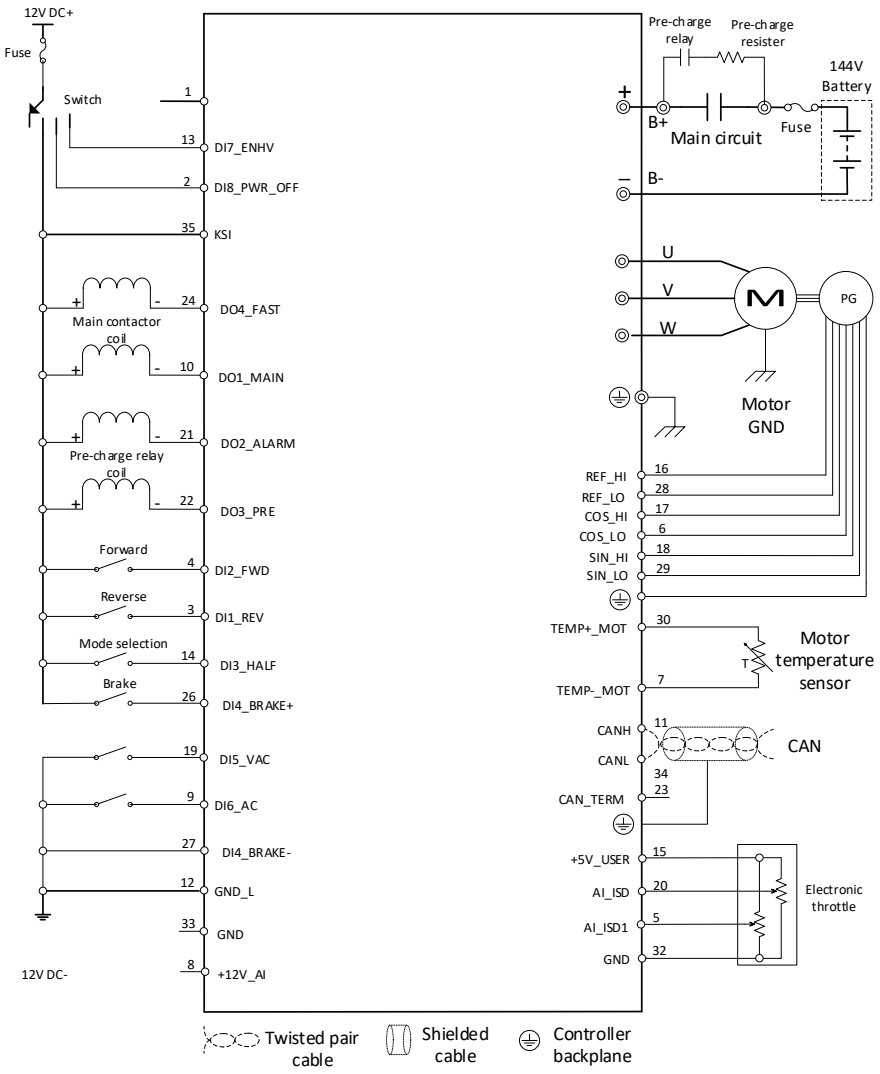

A.3 CAN Analyzer interface

DataSheet

USBCAN Interface

USBCAN-2A/Ⅱ/Ⅰ Intelligent CAN-bus Interface UM010206

Rev 2.00 Date:2/8/2007 **Product Data Sheet**

Overview

USBCAN-2A/Ⅱ/Ⅰ is an intelligent PC-CAN interface module which is compatible with USB1.1 and supports one or two CAN channels. Each channel integrates independent electrical isolation circuit. And with the module and USB port, a control node of CAN-bus can be formed by connecting the PC to the CAN network.

USBCAN-2A/Ⅱ/Ⅰ supports CAN2.0A/B protocol and different Baud rates from 5Kbps to 1Mbps, provides driver and software for multi-systems, truly satisfying all application requirements for customers and providing high reliability and efficiency solutions for industrial communications CAN network.

Features

- PC interface supports USB1.1 Protocol and can be worked with USB2.0;
- Integrated with one or two CAN-bus interface, supports CAN2.0A and CAN2.0B protocols, fully compatible with ISO/DIS 11898 standard;
- Programmable CAN-bus communication Baud rates from 5Kbps to 1Mbps;
- (DC+9V~+25V，200mA) from USB bus or external power supply;
- Adopts electrical isolation, the isolation voltage is : 2500Vrms;
- Max data flow for a single channel: 3000 fps (standard frame);
- Supports plug and play;

Applicable Field

- CAN-bus network diagnosis and test
- Auto electronic applications
- Electric power communication network
- Industrial control devices
- High-speed and large data communications

Order Info

TYPE	Temperature	Interface
USBCAN-2A	-25℃～+85℃	OPEN5
USBCAN-Ⅱ	0℃～+70℃	DB9
USBCAN-Ⅰ	0℃～+70℃	DB9

Typical Applications

Hardware

CAN controller: SJA1000T

CAN transceiver: PCA82C251

Interface

Bus: USB 1.1 (12Mbps)

Performance

Baud rate: 5Kbps ~ 1Mbps

Transfer rate: 3000 fps (standard frame)

Configuration

USB: interrupt and I/O are distributed by BIOS

Operation mode: normal, listen only 、self-transmitting and receiving

API: VCI function library

Operation system supported:

Windows98/Me/2000/XP/2003

Linux 2.4、Linux 2.6

Tools supported:

Testing tool for communication CAN: ZLGCANTest

OPC server: ZOPC Server

ICAN test tool: iCANTest

Virtual serial server: ZVCom

Power supply and environment

Power supply requirement: USB power supply, DC5V@200mA

External power supply: DC9V@200mA (Optional)

Operating temperature: -25°C ~ +85°C

Storage temperature: -40°C ~ +85°C

www.embedcontrol.com

ZHIYUAN Electronics Co., Ltd.

Industrial Control Department

ZHIYUAN ELECTRONICS

2.2 CAN-bus connector

USBCAN-Ⅱ module integrates two CAN-bus channels, while USBCAN-Ⅰ integrates one. USBCAN-Ⅱ/Ⅰ connects to CAN-bus network via DB9 male adapter or female adapter. CZ1 and CZ2 represent CAN channel numbers “0” and “1” respectively.

The pin signal definitions for DB9 conforms to DeviceNet and CANopen standards, see Table 2-1.

Notes: *USBCAN-Ⅰ interface module has two parallel DB9 male and female adapters, the pin sequence numbers for DB9 male adapter is opposite to those of DB9 female adapter. Please distinguish the pin numbers between the adapters.*

Table 2-1 : Signal Connections (DB9 adapter) for CAN-bus

DB9 male adapter	Pins	Signals	Descriptions
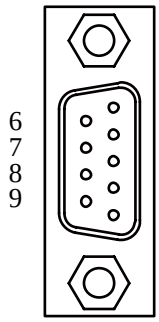	1	N.C.	unused
	2	CAN_L	CAN_L signal cable
	3	CAN_GND	Reference ground
	4	N.C.	unused
	5	CAN_SHIELD	Shield cable
	6	CAN_GND	Reference ground
	7	CAN_H	CAN_H signal cable
	8	N.C.	unused
	9	N.C.	unused

The CAN-bus signals from DB9 adapter can be switched to a 5-pin connector by using the optional DB9OPEN5 converter, making it much easier for connections.

Table 2-2 : Signal Assignment for DB9OPEN5 Converter

OPEN5 converter	Pins	Signals	Descriptions
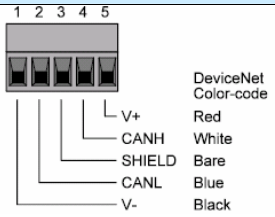	1	V-	Network power supply (negative pole)
	2	CAN_L	CAN_L signal cable
	3	SHIELD	Shield cable (FG)
	4	CAN_H	CAN_H signal cable
	5	V+	Network power supply (positive pole)

USBCAN-2A interface module supports two CAN channels that can be operated independently, and it can be used to connect to a CAN-bus network or CAN-bus interface device. The two channels can be pinned out by using a 10-pin plug-pull AWG 14-22 connector. The pins assignment is shown as Table 2-3.

A.4 Current Transducer

Current Transducer LA 50-S/SP1

I_{PN} = 50 A

For the electronic measurement of currents : DC, AC, pulsed..., with a galvanic isolation between the primary circuit (high power) and the secondary circuit (electronic circuit).

Electrical data

I_{PN}	Primary nominal r.m.s. current		50	A
I_P	Primary current, measuring range		0 .. ± 100	A
R_M	Measuring resistance		$R_{M\,min}$ $R_{M\,max}$	
	with ± 15 V	@ ± 50 A_{max}	0 330	Ω
		@ ± 100 A_{max}	0 100	Ω
I_{SN}	Secondary nominal r.m.s. current		25	mA
K_N	Conversion ratio		1 : 2000	
V_C	Supply voltage (± 5 %)		± 15	V
I_C	Current consumption		10 + I_S	mA
V_d	R.m.s. voltage for AC isolation test, 50 Hz, 1 min		3	kV

Accuracy - Dynamic performance data

X_G	Overall accuracy @ I_{PN}, T_A = 25°C		± 0.5		%
ε_L	Linearity		< 0.1		%
			Typ	Max	
I_O	Offset current @ I_P = 0, T_A = 25°C			± 0.1	mA
I_{OT}	Thermal drift of I_O	- 10°C .. + 70°C	± 0.2	± 0.4	mA
t_r	Response time [1] @ 90 % of I_{PN}		< 1		µs
di/dt	di/dt accurately followed		> 50		A/µs
f	Frequency bandwidth (- 1 dB)		DC .. 150		kHz

General data

T_A	Ambient operating temperature	- 10 .. + 70	°C
T_S	Ambient storage temperature	- 25 .. + 85	°C
R_S	Secondary coil resistance @ T_A = 70°C	130	Ω
m	Mass	45	g
	Standards [2]	EN 50178	

Features

- Closed loop (compensated) current transducer using the Hall effect
- Insulated plastic case recognized according to UL 94-V0.

Special features

- I_P = 0 .. ± 100 A
- K_N = 1 : 2000

Advantages

- Excellent accuracy
- Very good linearity
- Low temperature drift
- Optimized response time
- Wide frequency bandwidth
- No insertion losses
- High immunity to external interference
- Current overload capability.

Applications

- AC variable speed drives and servo motor drives
- Static converters for DC motor drives
- Battery supplied applications
- Uninterruptible Power Supplies (UPS)
- Switched Mode Power Supplies (SMPS)
- Power supplies for welding applications.

Notes : [1] With a di/dt of 50 A/µs
[2] A list of corresponding tests is available.

991014/5

Dimensions LA 50-S/SP1 (in mm. 1 mm = 0.0394 inch)

Front view

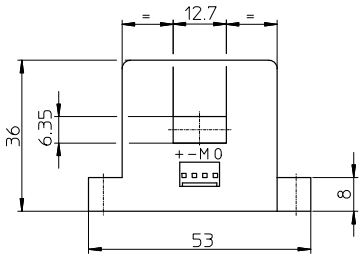

Left view

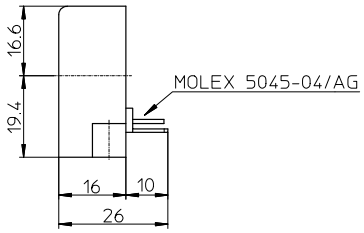

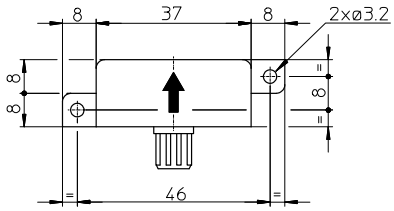

Top view

Secondary terminals

Terminal + : supply voltage + 15 V
Terminal - : supply voltage - 15 V
Terminal M : measure
Terminal 0 : NC

Connection

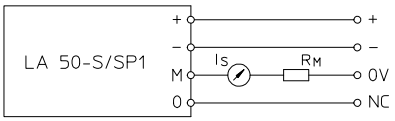

Mechanical characteristics

• General tolerance	± 0.2 mm
• Fastening	2 holes ∅ 3.2 mm
• Primary through-hole	12.7 x 6.35 mm
• Connection of secondary	Molex 5045-04/AG

Remarks

- I_S is positive when I_P flows in the direction of the arrow.
- Temperature of the primary conductor should not exceed 100°C.
- Dynamic performances (di/dt and response time) are best with a single bar completely filling the primary hole.
- In order to achieve the best magnetic coupling, the primary windings have to be wound over the top edge of the device.
- To measure nominal currents of less than 50 A, the optimum accuracy is obtained by having several primary turns (nominal current x number of turns < 50 At).

A.5 Core Material

Typical data for SURA® M235-35A

T	W/kg at 50 Hz	VA/kg at 50 Hz	A/m at 50 Hz	W/kg at 100 Hz	W/kg at 200 Hz	W/kg at 400 Hz	W/kg at 1000 Hz	W/kg at 2500 Hz
0,1	0,02	0,05	24,7	0,04	0,08	0,19	0,93	3,89
0,2	0,06	0,14	32,6	0,14	0,32	0,87	3,55	14,3
0,3	0,11	0,24	38,1	0,30	0,73	1,88	7,45	29,6
0,4	0,20	0,37	43,1	0,49	1,21	3,17	12,3	50,2
0,5	0,29	0,51	48,2	0,71	1,78	4,73	18,5	76,7
0,6	0,38	0,67	53,9	0,97	2,44	6,56	25,8	110
0,7	0,50	0,87	60,7	1,25	3,19	8,67	34,6	153
0,8	0,62	1,09	68,8	1,57	4,03	11,0	45,0	205
0,9	0,77	1,36	79,3	1,92	4,97	13,8	57,2	270
1,0	0,92	1,71	93,7	2,31	6,01	16,9	71,5	349
1,1	1,10	2,17	115	2,75	7,19	20,3	88,3	
1,2	1,31	2,89	156	3,26	8,54	24,3		
1,3	1,56	4,45	260	3,88	10,1	28,9		
1,4	1,92	10,3	690	4,67	12,2	34,8		
1,5	2,25	32,4	1950	5,54	14,4	41,2		
1,6	2,53	84,6	4410					
1,7	2,75	162	7630					
1,8	2,94	274	12000					

Loss at 1.5 T , 50 Hz, W/kg	2,25
Loss at 1.0 T , 50 Hz, W/kg	0,92
Anisotropy of loss, %	10
Magnetic polarization at 50 Hz	
H = 2500 A/m, T	1,53
H = 5000 A/m, T	1,64
H = 10000 A/m, T	1,76
Coercivity (DC), A/m	35
Relative permeability at 1.5 T	610
Resistivity, μΩcm	59
Yield strength, N/mm²	460
Tensile strength, N/mm²	580
Young's modulus, RD, N/mm²	185 000
Young's modulus, TD, N/mm²	200 000
Hardness HV5 (VPN)	220

RD represents the rolling direction
TD represents the transverse direction
Values for yield strength (0.2 % proof strength)
and tensile strength are given for the rolling direction
Values for the transverse direction are approximately 5% higher

cogent
Surahammars Bruks AB

June 2008